2010

The characterisation of planar silicon pin diodes for use in proton therapy

Joel Poder
University of Wollongong

The Characterisation of Planar Silicon PIN Diodes for Use in Proton Therapy

Joel Poder

This thesis is presented as part of the requirements for the award of the Degree of:

Master of Science - Research
of the Centre Of Medical Radiation Physics,
University of Wollongong

2010

CERTIFICATION

I, Joel Poder, declare that this thesis, submitted in partial fulfilment of the requirements for the award of Master of Science – Research, in the Centre for Medical Radiation Physics, University of Wollongong is wholly my own work unless otherwise referenced or acknowledged. This document has not been submitted for qualifications at any other academic institution.

Joel Poder
28th June 2010

ABSTRACT

Many new techniques in the delivery of radiation therapy are being developed for the treatment of cancer. One of these new techniques, proton therapy is becoming increasingly popular due to the presence of the characteristic proton Bragg peak, which allows for better conformation of the dose to the tumour volume. The production of high LET secondary particles in the beam line and within the patient however could result in a significant contribution to the integral dose and diminish this potential advantage. Measured secondary particle doses from clinical proton facilities vary greatly; this is partly due to the differences in beam delivery methods at different centres and due also to the different methods used to measure this secondary particle dose.

The potential of quantification of this mixed particle dose can be achieved through practical and simple measurements of non-ionizing energy losses (NIEL) and ionizing energy losses (IEL). The suitable sensor for NIEL measurements is a silicon PIN diode, through the development of the silicon PIN diodes the possibility of the quantification and therefore significance of the dose delivered by the primary and secondary particles can be realised.

This thesis investigates the characterisation of the response of silicon PIN diodes for use in proton therapy, of particular interest is the in field forward bias response of the PIN diodes as well as their dependence on temperature and light.

Monte Carlo calculations are performed using the Geant4 platform to characterise the response of the silicon PIN diodes when placed in field during proton therapy. The forward bias response of the detector when placed in field was found to be dependent on protons only, with the neutron component of the response being negligible. This allows for the possibility of characterisation of the PIN diodes on the central axis of the beam.

The relative sensitivity of the PIN diodes to protons was found by dividing the forward bias response by the theoretical depth dose and it was found that the relative

sensitivity of the diode is independent of the phantom material and depends only on the initial energy of the primary proton beam.

Experiments are performed in order to characterise the response of the PIN diodes under various conditions. The effect on the forward bias response of the PIN diodes when exposed to visible light was examined by taking forward voltage measurements on each of the diodes both exposed and not exposed to visible light. It was found that the difference in forward bias voltage measurements with light incident on the diode and when light is blocked is no greater than the uncertainty involved in the measurement, using the dedicated forward bias voltage read – out system.

In order to investigate any change in forward bias voltage across the temperature range of interest each of the PIN diodes forward bias voltage is measured over a range from 25 - 35°C. The average temperature coefficient was found to be 0.75mV/°C at 1mA and 1.8mV/°C at 20mA. Considering that the variation in room temperature was expected to be minimal (< 1°C) the temperature of the diodes should differ very little over the several hours between pre and post irradiation read out.

The linearity of the current source in the read-out system is tested at current values of 1, 10, 15 and 20 mA over a wide range of resistances to ensure that the current remained constant over these values. A change in the linear relationship between voltage and resistance was observed in the 10, 15 and 20 mA characteristics. This change was attributed to the fact that the current source is no longer putting out a constant value, highlighting the limit of power in the forward bias voltage read-out device.

ACKNOWLEDGEMENTS

I would firstly like to thank my supervisor Professor Anatoly Rozenfeld for his ongoing support, both scientifically and financially, throughout the duration of this project. I would also like to take this opportunity to thank Professor Rozenfeld and all other staff of the Department of Engineering Physics and the Centre for Medical Radiation Physics (CMRP) for their contribution made towards my education in field of Medical Physics and giving me the opportunity to begin a career in this field. I am grateful to have collaborated with many of the members of staff during my time at the University of Wollongong.

I would like to acknowledge the contribution made by my co-supervisors Dr Susanna Guatelli and PHD Candidate Stephen Dowdell, specifically for the time and effort they dedicated in assisting with the development of the Monte Carlo applications presented in this thesis. Their availability for my day to day enquiries, and the ideas they proposed regarding the development of these applications was invaluable and is much appreciated.

I would like to acknowledge the staff and students from the Australian Nuclear Science and Technology Organisation (ANSTO) Detector Research Laboratory: PHD candidate Amy Ziebell for her ideas and support with respect to the experimental components of this thesis, Dr. Mark Reinhard for his expertise in the use of the silicon PIN diodes and Mr. Adam Sarbutt for his assistance with the technical aspects of the detector electronics.

I thank also the laboratory staff of the CMRP Mr. Peter Ihnat and Mr. Terry Braddock as well as research fellows Dr. Marco Petasecca and Mr. Dean Cutajar for their support and expertise.

Finally, thank you to my family, friends and fellow students who have supported me and shown great patience during those stressful times that I have encountered throughout this project.

TABLE OF CONTENTS

LIST OF FIGURES

LIST OF TABLES

1. INTRODUCTION

1. 1 Vision of the Project

The vision of this project is to predict the relative response of forward biased silicon PIN diodes for use in proton therapy, through the development of a system based on semiconductor detectors. If the vision of this project is realised the diodes have the potential use for separation of components the mixed proton neutron doses experienced in proton therapy. Therefore the diodes could potentially assist in the quantification of the dose delivered out-of-field in these proton therapy fields and contribute towards quality assurance procedures and estimation of neutron risk associated with proton therapy delivery.

1. 2 Motivation

Measured secondary particle doses from clinical proton facilities vary greatly; this is partly due to the differences in beam delivery methods at different centres and due also to the different methods used to measure this secondary particle dose. The number of proton therapy facilities worldwide is growing rapidly [9] and the debate regarding the significance of these secondary particles (in particular neutrons) to the total dose is still a topic of debate in the literature [10], [11], [12], [6]. The contribution of neutrons to this total dose is particularly significant due to their relatively large range in tissue and their deposition of dose via charged particles of high linear energy transfer (LET). LET is a measure of energy transferred to a material as a charged particle passes through it. Through the development of the silicon PIN diodes the possibility of the quantification and therefore significance of the dose delivered by the primary and secondary particles can be realised, through the separation of dose delivered from protons and neutrons. This will therefore contribute towards the prediction of the risk of developing secondary cancer from this secondary particle dose.

1. 3 **Thesis Outline**

The aim of this thesis is to continue research into the characterisation of the response of silicon PIN diodes for use in proton therapy. A new approach for the separation of secondary particle dose was considered. This approach was based on a dual detector method, represented either by a single PIN diode working in non-ionizing and ionizing energy mode simultaneously, or by a PIN diode working in combination with a tissue equivalent ionization chamber. Monte Carlo calculations are used extensively throughout this thesis and therefore Chapter 3 is dedicated to providing an introduction to the Monte Carlo method and a description the Geant4 toolkit.

Chapter 4 describes the various experiments performed in order to characterise the response of the PIN diodes under various conditions and testing of the read-out system used with the diodes. The dependence of the forward bias response of the diodes on temperature as well as visible light is described as is the linearity of the read-out system over a wide range of resistances. The experiments are performed in order to estimate the uncertainty in measurements as a result of changes in these parameters.

Chapter 5 is dedicated to the description of Monte Carlo calculations using the Geant4 platform used to characterise the response of the silicon PIN diodes when placed in-field during proton therapy. The forward bias response due to protons and neutrons is investigated as is the depth dose profile of the beam. The responses of the PIN diodes are then theoretically predicted and results compared with experimental measurements.

2 LITERATURE REVIEW & BACKGROUND

2. 1 **Proton Therapy**

2.1.1 Introduction to Proton Therapy

Over the last two decades external beam radiation therapy has been a mainstay of cancer treatment and cure around the world. During this time period sophisticated techniques such as intensity modulated radiation therapy (IMRT) and proton therapy have evolved, allowing for conformal dose delivery.

Proton therapy is becoming increasingly popular due to its ability to provide highly conformal dose distributions, thereby sparing healthy tissues and resulting in a potentially lower whole-body dose. The potential for improvement may be based on exploiting features of the Bragg peak in the proton beam [2]. The Bragg peak is the phenomenon where the absorbed dose deposited by protons increases significantly at the end of the proton range; this gives rise to a maximum dose at a depth which is greater than the entrance dose. A typical Bragg peak is shown in Figure 2.1. The protons range is also well defined and depends on the initial energy of the protons. There is a sharp dose fall off distal to the Bragg peak, scattering in tissue produces a small penumbra [2], [13], [14], [9].

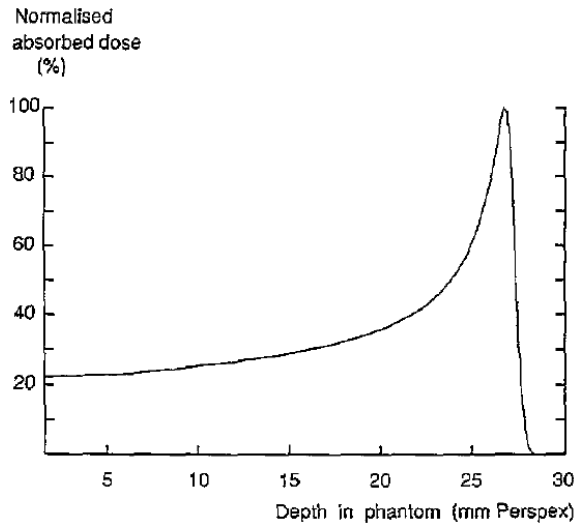

Figure 2.1 A typical proton Bragg peak. 62 MeV proton beam [2].

In order to provide uniform coverage over the tumour target, it is necessary to spread out the initially narrow pencil beam through the use of a number of beam modifying devices. Most of the current proton therapy facilities achieve this through by inserting a scattering material into the beam path (passive scattering). These passive systems are based entirely on absorbers, scattering foils and collimators, whose thickness and shape are designed to provide the desired angular and energy distribution of the beam [10]. The proton field is conformed to the tumour shape through the use of collimators. The conformality in depth is achieved through the use of a rotating wheel of variable thickness called a range modulator [10]. This is necessary in order to achieve a homogeneous dose in the target volume and a sharp dose falloff at the distal edges of the target. Additionally, for each patient, individual compensators must be fixed in the proton beam path in order to conform the distal dose falloff to the target volume [8].

Another delivery technique used for proton therapy is known the scanning technique. This technique utilises a system of deflection magnets to scan the tumour in the direction normal to the beam axis. In order to achieve the desired depth distribution using a cyclotron a passive range modulator can be used, although if a synchrotron is used for the source of the protons modulation can be performed by continuously varying the extraction energy [10]. Thus, there is no need for scattering, flattening and compensating devices in this method [8]. In the method of spot scanning the

tumour is subdivided into volume elements where single spot irradiations are carried out during treatment [15]. Other methods of scanning used in proton therapy are uniform scanning [16] and wobbling [17].

As passive scattering necessarily introduces a number of material components into the beam line, proton interactions with these components can result in the production of high-energy secondary neutrons. In clinical passively scattered proton beams, the largest source of these neutrons, in terms of flux, is the range modulator wheel [18]. However, most of these secondary neutrons are absorbed by other beam modifying devices before reaching the patient [18]. The final collimator, located close to the patient is also a large source of neutrons. This collimator is fabricated out of brass with a patient specific aperture shaped to match the target [12]. As well as these secondary neutrons, depending on the beam entry point, the patient may extend beyond the shadow of the final collimator and elastically scattered protons deflected out of the defined field will pose a potential treatment hazard [11]. Due to the absence of scattering materials in the beam line in active scanning, mostly neutrons produced by the proton beam within the patient contribute to secondary dose [8]. Therefore, the spot scanning method is expected to have a much lower neutron doses than passive scanning [8].

2.1.2 Secondary Particles in Proton Therapy

Measured secondary particle doses from clinical proton facilities vary greatly; in part due to the use of different measuring techniques. The production of secondary neutrons also depends strongly on beam geometry and at present, there is no standard configuration for beam geometries and materials in the beam path [10]. These secondary neutrons and protons, originating from elastic nuclear collisions both in the beam line and within the patient are of interest for a number of reasons. Firstly, it needs to be considered whether all nuclear reaction products deliver a significant contribution to the total dose. Also, there could be an enhanced relative biological effectiveness (RBE) due to low energy and/or heavy secondaries. Finally, neutrons and protons originating from nuclear interactions may deliver dose outside the target volume [6].

Non-elastic nuclear interactions between protons and the target nucleus within the patient produce particles such as neutrons, alpha particles, and recoil protons which can have high LET. These particles can affect the dose distribution and biological effectiveness of the beam [5]. Wroe *et. al.* [5] studied the dosimetric effect of these interactions by means of Monte Carlo simulations. The results highlighted the importance of the nuclear interactions in determining the amplitude and position of the Bragg Peak as well as the peak to entrance dose ratio. The study was carried out for monoenergetic 60 and 200 MeV proton beams within a number of different phantoms. The results obtained for the 200MeV proton beam are shown in Figure 2.2.

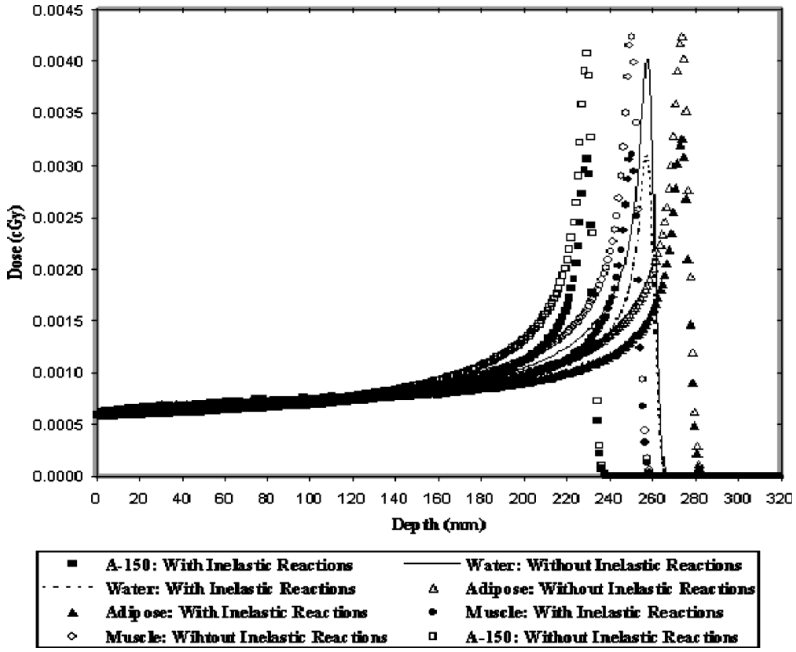

Figure 2.2 Comparison of depth dose distributions for a mono-energetic 200 MeV proton beam incident on a number of different phantom materials [5].

Figure 2.2 shows the effect non-elastic reactions have on the amplitude of the Bragg peak. A decrease in peak to entrance dose ratio was observed to be approximately 5-8% for 60 MeV protons and greater than 30% for the 200 MeV beam. The dose distribution depends on the phantom material and the energy of the incident proton beam.

In the case of the simulation that included non-elastic reactions, some dose is deposited distal to the Bragg peak due to long-range non-elastic products such as neutrons and photons. The absorbed dose distal to the Bragg Peak is orders of magnitude smaller than the peak dose; however, it may be important to consider this dose due to the possible high RBE of some of the secondary particles, especially for treatment of tumours close to the critical organs where proton therapy has a great advantage. Additionally, the superposition of a number of peaks in order to form the superimposed Bragg peak will result in a superposition of this tail. This could result in a biologically significant dose to sensitive structures situated beyond the Bragg peak as the particles present in this region have a high LET [5].

Paganetti [15] studied theoretically the particle yield from different nuclear interactions, as a function of proton penetration depth, and for different proton beam energies. Three-dimensional dose distributions from primary and secondary particles were simulated for a superimposed Bragg peak, in a phantom (size 3 x 3 x 3 cm^3) originated by an un-modulated 160 MeV proton beam.

The simulated two dimensional spread out Bragg peak is shown in Figure 2.3 together with the contributions of various dose components, deriving from different particles. The dose contribution from ^{3}He and α-particles is below 0.2% and the contribution of secondary protons is about 5% at the proximal edge of the superimposed Bragg peak [6].

The dose deposited distal to the Bragg peak was also calculated for beams with energies of 160, 190, 220 and 250 MeV. It was found that the dose in this region was mainly delivered by protons generated by secondary neutrons via the (n,p) reaction and the dose deposited decreased exponentially as a function of depth. The neutron dose lateral to the target volume was found to be in the same order of magnitude as the distal area behind the Bragg peak [6]. The contribution of nuclear secondaries rises in this area because the primary proton fluence is decreasing rapidly whereas there is a contribution of secondary protons from (n, np) reactions [6]. The situation in the region distal to the Bragg Peak is similar to the plateau region of the Bragg peak where the high-LET components are entirely due to secondary particles, but

opposite to the peak area where the fluence of secondaries is much lower than the primary proton fluence [6].

Since the neutron dose depends on the number of initial protons incident on the irradiated volume, the dose also depends on the treatment volume. Zheng *et al.* [7] aimed to estimate the neutron dose equivalent per therapeutic absorbed dose (H/D) as a function of field size. Monte Carlo methods were used in order to estimate the neutron dose equivalent (H) and therapeutic absorbed dose (D), as well as the distribution of dose equivalent in neutron energy H(E) [7].

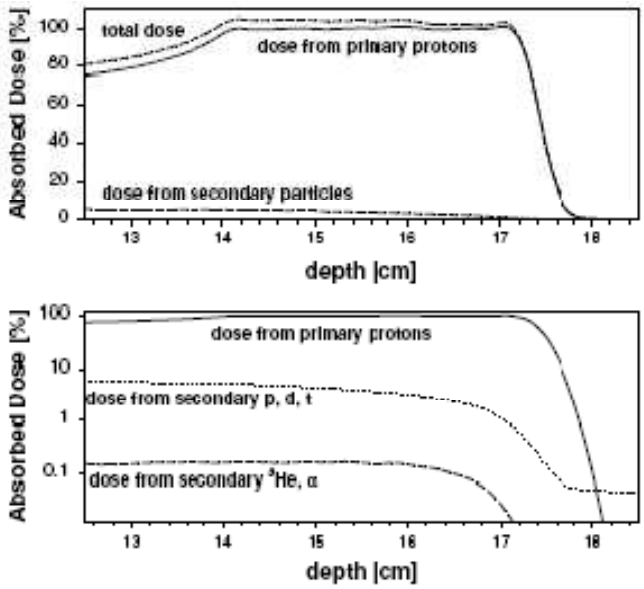

Figure 2.3 Depth dose distributions for a modulated 160 MeV proton beam incident on a water phantom in linear scale (upper figure) and in a logarithmic scale showing contributions of heavier secondary particles (lower figure) [5].

To assess the influence of proton field size on the neutron dose equivalent the ratio of neutron equivalent dose to therapeutic absorbed dose, values for specific field sizes with the H/D value of a field size of zero were examined. It was found that when the aperture size was decreased from 18x18 cm^2 to 10x10 cm^2 the neutron dose equivalent increased by approximately 29% at isocentre, 33% at 150cm distal to the isocentre and 9% at 150cm lateral from the isocentre [7]. As the collimating aperture size increased, a greater number of protons escaped from the nozzle without producing neutrons.

The energy weighted neutron fluence and neutron dose equivalent spectra are shown in Figures 2.4 and 2.5 respectively. High-energy neutrons produced from direct (nucleon-nucleon) reactions contribute to about one-half of the neutron dose equivalent and isotropically emitted low energy neutrons from evaporation processes contribute to about one-third of the dose equivalent [7].

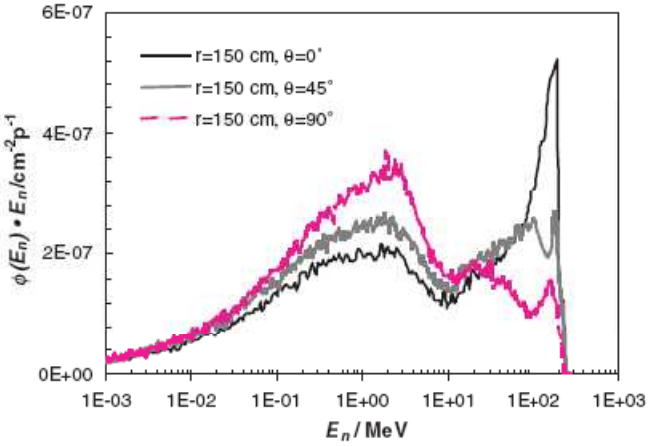

Figure 2.4 Energy-weighted neutron fluence spectra ($\Phi(E_n).E_n$) as a function of neutron energy (E_n) around a passive scattering nozzle, with a 250MeV beam entering the nozzle using a closed final proton collimating aperture [7].

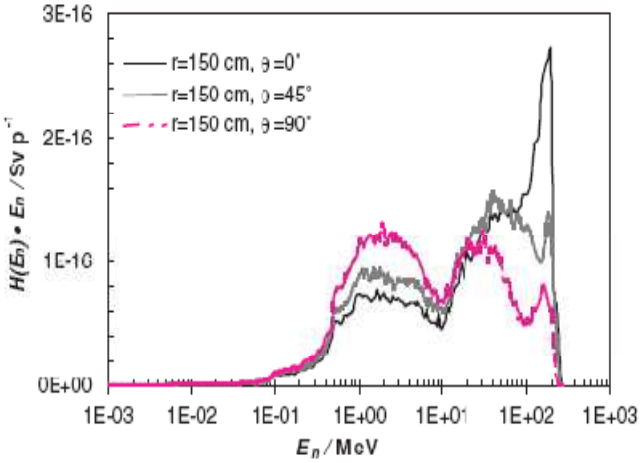

Figure 2.5 Energy-weighted neutron dose equivalent spectra ($H(E_n).E_n$) as a function of neutron energy (E_n) around a passive scattering nozzle, with a 250MeV beam entering the nozzle using a closed final proton collimating aperture [7].

Since the high energy component is forward peaked, it can be seen to fall off rapidly as distance from the beam axis increased (θ is increased from 0 to 90°). Also, the evaporation process is isotropic, so the low-energy component varies mainly with nozzle to receptor distance. At a fixed isocenter to receptor distance (r = 150cm) the nozzle to receptor distance decreases only slightly as θ increases from 0 to 90°. This results in a slight increase in the magnitude of the low energy peak at large angles [7].

An article published by Binns and Hough [11] achieved similar results to those found by Zheng *et al.* using a spherical tissue-equivalent proportional counter. A fast neutron dose component was identified at the patient position that decreased progressively with lateral displacement and radial distance from the final collimator. Also, extending beyond the periphery of the patient collimator a forward peaked cone of scattered high energy protons was evident [11]. The neutron spectral fluencies were also investigated by Yan *et al.* in several locations out of field with Bonner sphere measurements and established by unfolding techniques [19], however these measurements were done outside of the phantom and in free air geometry.

Other measurements have been performed to assess the dose equivalent outside the primary proton treatment field. Wroe *et al.* [4] used a silicon-on-insulator (SOI) microdosimeter placed at several positions both in and on the surface of an anthropomorphic phantom to determine the dose equivalent as a function of depth and lateral distance from the primary field edge [4].

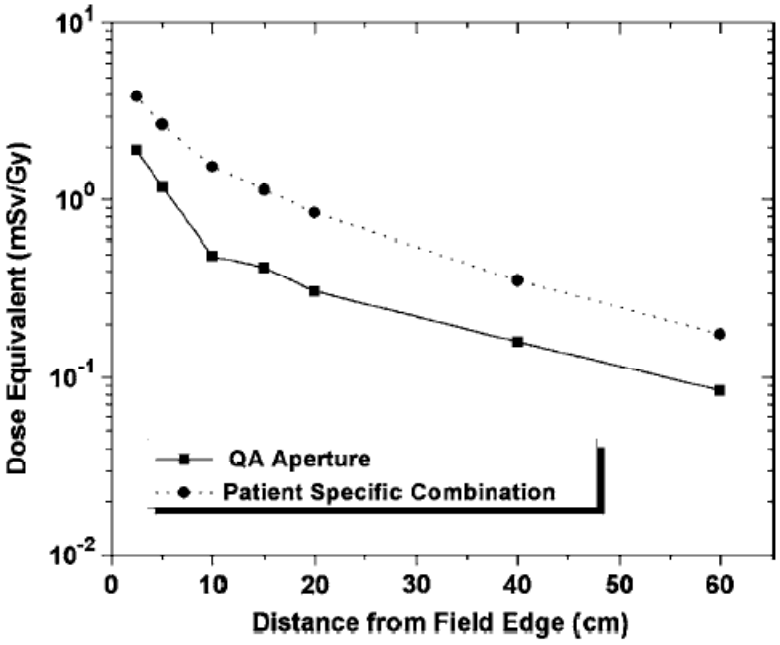

Figure 2.6 Results measured with the SOI microdosimeter for both a patient specific aperture/bolus portal and a 13cm circular QA aperture with no bolus present [4].

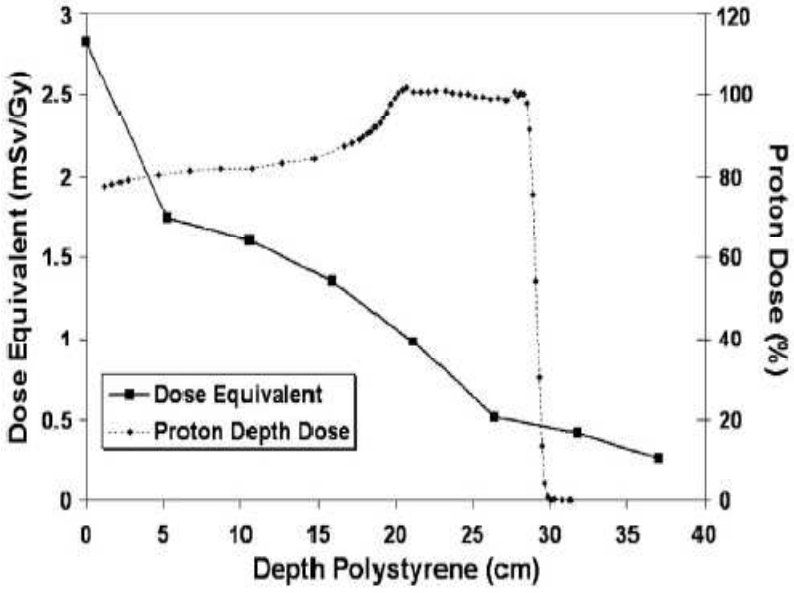

Figure 2.7 Dose equivalent at 5 cm from the field edge compared with the depth dose distribution of the proton beam as measured along the central axis with a Markus chamber [4].

It is evident from the results that the aperture and bolus used within a typical treatment can affect the dose equivalent. The increased collimation present in the case of the patient specific aperture resulted in a greater interaction of the primary proton beam with the collimator, leading to increased dose equivalent outside the treatment field [4]. Figure 2.7 shows that the initial dose equivalent values at the surface of the phantom decreased by 38% after traversing 5 cm of phantom material. Thus, it can be concluded that many secondary particles produced within the passive scattering system do not penetrate to a great depth within the phantom and such particles are most likely to be thermal neutrons [4].

In work published by Agesteo *et al.* [10] three different existing beam delivery configurations are considered and the neutron and photon dose estimated with Monte Carlo simulations. The work considered an eye treatment facility (65 MeV) which utilises a passive beam delivery system, a 200 MeV passive scattering system for deep-seated tumours, and a 200 MeV isocentric gantry with an active system performing three-dimensional conformal irradiation [10].

The dependence of the absorbed dose due to secondaries is dependent on the energy of the primary proton beam. This was evident in the results achieved by Agesteo et al. as the dose due to secondaries was found to be larger for the scanned proton beam used for treating deep-seated tumours than for the passive beam system related to eye treatment where the passive beam used for eye treatment has a lower primary proton energy than the scanned beam [10].

Schneider *et al.* further investigated the dose due to secondary's when using the spot scanning technique [8]. Measurements of the secondary neutron dose were performed during irradiation of a water phantom with 177 MeV protons using a Bonner sphere. These measurements were compared with the results of Monte Carlo simulations. The results obtained when measuring at different distances from the central axis were compared with the data published by Binns and Hough [11]. The results of the comparison can be seen in Figure 2.8.

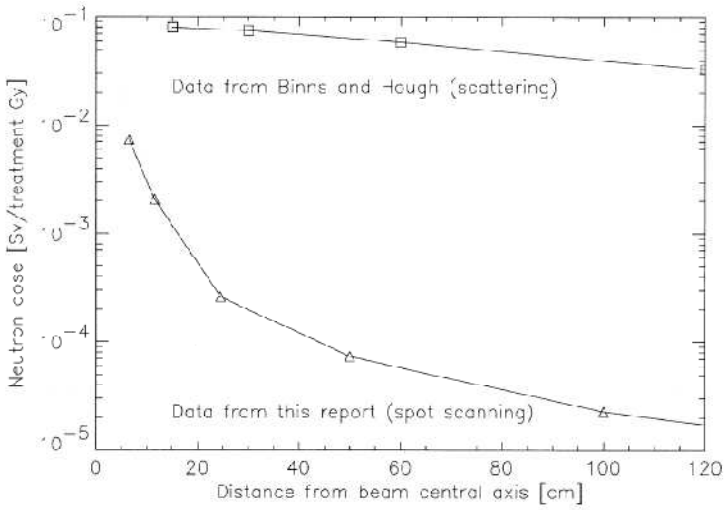

Figure 2.8 Plot of the measured neutron ambient dose equivalent as a function of lateral distance from the beam. The squares correspond to measurements in a scatter beam line, the triangles correspond to measurements obtained at a spot scanning beam line [8].

Figure 2.8 shows the advantage of using the spot scanning technique increases with the distance from the beam. The steeper gradient in the spot scanning curve stems from the fact that a considerable number of neutrons are produced in the water phantom; however in the experiment of Binns and Hough, no phantom was irradiated and a flatter gradient on the curve can be seen [8]. Schneider *et al.* concluded from these measurements that the dose deposited by secondary neutrons during proton radiotherapy using the spot scanning technique can be neglected in the treatment region.

2.1.3 Risk of Secondary Cancer in Proton Therapy

As well as quantifying the dose due to secondary particles there has been significant research conducted in estimating the risk of developing second cancer from this dose [15], [12]. Brenner and Hall used estimated neutron dose equivalent to relevant organs to calculate lifetime cancer risks. They employed standard techniques, such as those described in the US National Academy of Sciences BEIR-VII report [3].

In order to estimate a cancer risk from these secondary particles, in particular neutrons, an RBE factor must be applied to standard low-LET cancer risk estimates.

In general, this RBE is both dose and energy dependent. This results in relatively uncertain values for neutron RBE's, as all available human and animal data from neutron carcinogenesis may be derived from fission neutrons with energy lower than 10 MeV [12]. In contrast, neutrons produced in a proton therapy context are predominantly of high energy with more than two-thirds of the neutron dose coming from neutrons with energies greater than 100 MeV [3]. Figure 2.9 below shows the total estimated cancer risks (over all organs) as a function of age for both males and females. These results were confirmed by a study by Jarlskog and Paganetti [20].

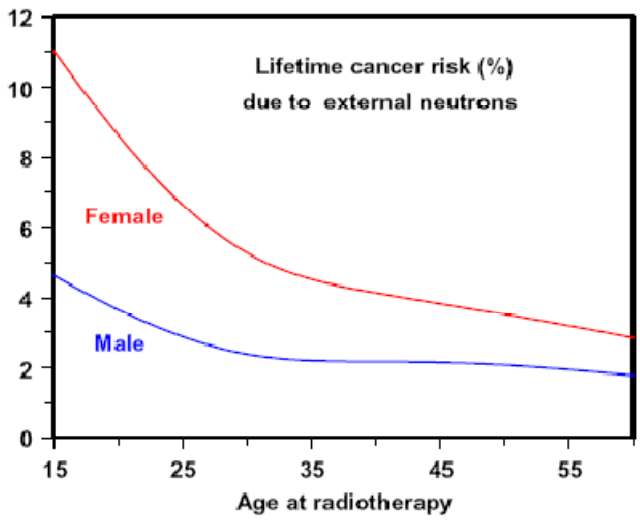

Figure 2.9 Total estimated lifetime second cancer risks due to externally produced neutrons, for a 72Gy proton therapy lung-tumour plan at a passively scattered facility [3].

Zacharatou Jarlskog and Paganetti [15] followed the same approach as above by using the BEIR-VII Report [3] to estimate second cancer risks through functional relationships between radiation dose and induced cancer. Monte Carlo simulations were used to gain the neutron data and similar results to Brenner and Hall [12] were achieved.

It was found that the female had significantly greater lifetime attributable risk values than the male (approximately a factor of 2.5). The risk was also found to decrease rapidly with age at exposure, with the lifetime attributable risk for a 9 month old boy and 39 year old at 1-2% and 0.1-0.2% respectively [15]. The research also found that neutrons generated in the treatment nozzle, including all patient specific devices

were responsible for 82-98% of the total risk, depending on the proton beam properties [15].

2. 2 **Monte Carlo Methods**

The Monte Carlo technique has become ubiquitous in medical physics in the last 50 years [21]. In medical physics Monte Carlo codes are widely used to solve dosimetric problems in radiotherapy, radiation protection, and diagnostic x-ray applications [21]. They are also used to characterise and optimise detector specifications for use in dosimetry. As computing power continues to increase the possibility of using Monte Carlo techniques for treatment planning is becoming increasingly feasible. Monte Carlo simulations are able to calculate accurately dosimetric quantities of interest, with no approximations. However the execution time of Monte Carlo simulations are often prohibitive for the use of Monte Carlo calculations in clinical circumstances. Solutions to provide a quick simulation response are one of the objects of current computing research, as parallelised execution of simulations on clusters of computers or execution on GPU.

In medical physics, a number of different radiation transport codes are available for use. I adopted Geant4, as it is an open-source, multi-purpose Monte Carlo simulation toolkit.

2.2.1 The Geant4 Monte Carlo Simulation Toolkit

The GEANT4 toolkit is a general purpose code developed for particle physics applications describing the interactions of particle with matter. It is able to simulate the transport of many particle types and has previously been used for a variety of applications in radiotherapy physics, high energy physics and radiation protection in space [21]. It provides basic functionality of simulation as to describe detector geometry and materials, to transport particle momentum, to describe detector response and to visualise simulation experimental set-up and particle tracks. It also provides an extensive set of physics models, to describe interactions of particles with

matter across a wide energy range [22]. By using object oriented technology and C++ language, a flexible and extensible simulation toolkit has been created.

GEANT4 has a wide range of applications in medical physics. It is currently used in radiotherapy with external photon beams in order to plan treatments [23]. Starting from a CT image it is possible to perform a patient dedicated treatment plan to simulate the correct dose distribution on the target [24]. Many other significant activities are in progress in the medical physics field both in diagnostic (e.g. PET) and therapy (e.g. IMRT and hadron therapy).

2. 3 **Semiconductor Detectors**

The use of a solid detection medium is beneficial in many radiation detection applications. This is due to their superior energy resolution, compact size, relatively fast timing characteristics and an effective thickness that can be varied to match the requirements of the application [25].

When a charged particle passes through a semiconductor the overall significant effect is the production of many electron-hole pairs along the track of the particle. The electric field that exists at the junction of semiconductor diode detectors causes any electrons (and therefore holes) created in or near the junction to be swept towards the n-type and p-type regions of the detector respectively. This motion that constitutes the basic electrical signal created when charged particles interact with the detector.

If the situation is reversed, and the *p* side of the junction is made more negative with respect to the *n* side, the junction is reversed biased. Under these circumstances, it is the minority carriers that are attracted across the junction and, because their concentration is relatively low, the reverse current across the diode is quite small. A reverse biased diode makes an attractive radiation detector because charge carriers created within the depletion region can be quickly and efficiently collected.

At any nonzero temperature, some thermal energy is shared by the electrons in the crystal. It is possible for a valence electron to gain sufficient thermal energy to be

elevated across the bandgap into the conduction band. Physically, this process simply represents the excitation of an electron that is normally part of a covalent bond such that it can leave the specific bonding site and drift throughout the crystal. The electron in the conduction band can be made to move under the influence of an applied electric field. The hole, which is created when the excited electron leaves a vacancy in the valence band, will also tend to move in an electric field, but in a direction opposite to that of the electron. The motion of both these charges contributes to the observed conductivity of the material [25].

The probability per unit time that an electron-hole pair is thermally generated is given by

$$p(T) = CT^{3/2}\exp\left(-\frac{E_g}{2kT}\right) \quad (2)$$

Where T is the absolute temperature, E_g is the bandgap energy, k is Boltzmann's constant and C is a proportionality constant characteristic of the material. As reflected in the exponential term, the probability of thermal excitation is critically dependent on the ratio of the bandgap energy to the absolute temperature. In the absence of an applied electric field, the thermally created electron hole pairs ultimately recombine, and equilibrium is established in which the concentration of electron hole pairs observed at any given time is proportional to the rate of formation [25].

2.3.1 PIN Diodes

PIN diodes were investigated as detectors for mixed radiations fields in proton therapy [26]. In many applications electronic devices are operated in mixed radiation fields. In such fields, the operating lifetime is difficult to predict due to the different damage mechanisms resulting from exposure to various components of the radiation field [27]. The main mechanisms of damage by radiation in silicon devices are due to the deposition of ionizing and non-ionizing energy. Practical and simple measurements of non-ionizing energy losses (NIEL) and ionizing energy losses (IEL) in neutron and proton fields is an important issue for quality assurance in the radiation environment at different radiation facilities [28].

NIEL are proportional to the bulk radiation damage in semiconductor devices resulting from displacement of atoms from their sites. For NIEL, the silicon device effects are understood in terms of displacement KERMA (kinetic energy released per unit mass) in silicon. The change in electrical characteristics acts as a suitable monitor of NIEL in devices affected by such atomic displacement which are producing spectra of localised energy centres in a forbidden gap acting as recombination centres and concentration compensation centres in a bulk of Si device. The forward voltage of the PIN diode increases due to radiation degradation of the carrier lifetime and the changing resistivity of the material. Detailed theory of the forward voltage mode PIN diode response to neutrons can be found in [29], [30] and [28].

A specially designed planar Si PIN diode operated in forward bias mode can be sensitive for NIEL measurements and was successfully applied for fast neutron dosimetry in mixed gamma neutron fields including fast neutron therapy and 1MeV(Si) neutron equivalent fluence [29], [31], [32], [33] [34]. The advantage of the PIN dosimetric diode operated in a forward voltage mode of operation is that its response is almost insensitive to gamma radiation and has much less sensitivity to protons per unit of tissue absorbed doses in comparison with neutrons. The response of the PIN diode in mixed neutron-proton-gamma field when operated in forward bias mode is given by

$$\Delta V_f = C_{fp}\left(Dp_p + Dp_n\right) + \beta \int_0^\infty K_{Si}(E_n)\Phi(E_n)dE_n, \quad (3)$$

where Dp_p and Dp_n are the respective absorbed tissue doses from protons produced by protons and protons produced by neutrons, C_{fp} and β are constants, $K_{Si}(E_n)$ is the neutron damage KERMA in silicon as a function of neutron energy, $\Phi(E_n)$ is the neutron fluence as a function of energy and ΔV_f is the shift in forward voltage of the detector due to NIEL.

It is discussed in [28], [29] and [30] that the ratio of neutron damage KERMA in silicon and neutron damage KERMA in water is approximately constant for neutron energies above 250 keV. That is,

$$\frac{K_{Si,n}^{damage}}{K_{water,n}^{damage}} = const. \tag{4}$$

This means that it is possible to approximate $\int_0^\infty K_{Si}(E_n)\Phi(E_n)dE_n$ as αD_n. Equation 3 now becomes

$$\Delta V_f = C_{fp}Dp_p + C_{fp}Dp_n + \beta\alpha D_n. \tag{5}$$

Finally, as the absorbed dose deposited by protons produced by neutrons can be attributed to neutrons, then $Dp_n \approx D_n$ and equation 5 becomes

$$\Delta V_f = C_{fp}Dp_p + (C_{fp} + C_{fn})D_n, \tag{6}$$

where $\alpha\beta = C_{fn}$. The same detector can also be used for IEL measurements. When operated in a current mode (reverse bias) the detector acts as a charge collector, its response when operated in this mode is given by

$$I_\gamma = C_{\gamma p}(\dot{D}p_p + \dot{D}p_n), \tag{7}$$

where I_γ is the current mode response of the detector due to IEL, $C_{\gamma p}$ is a constant, and $\dot{D}p_p$ and $\dot{D}p_n$ are the dose rates due to protons and neutrons respectively. This equation is valid assuming charge-equilibrium conditions are met; the typical thickness of the silicon PIN diodes is 350 μm [35], which corresponds to proton energies of approximately 0.15 MeV. Considering that in proton therapy, the average energy of protons at all depths is much greater than this value [11], charge-equilibrium conditions are achieved. Thus, a dual detector system is able to be realised with the one diode by solving equations 6 and 7 simultaneously and separating the mixed field dose.

Silicon diodes in a current (IEL) mode are used for relative absorbed dosimetry in proton therapy and demonstrated good agreement with ionization chamber measurements [36]. Some disagreement was observed in a peak of the Bragg dose curve that is related to dose rate effect in some diodes and difference in sizes between diodes and ionization chambers.

These planar and bulk silicon PIN diodes have been developed at the Centre for Medical Radiation Physics (CMRP) at the University of Wollongong (UOW). Measurements with these diodes in a neutron field were carried out in order to understand the effect of geometry on the response of the diodes [28]. It was demonstrated that the circular planar diodes have predictable t^2 sensitivity where t is the radial distance between the p^+ core and n^+ periphery of the PIN structure. The effect of NIEL damage due to neutrons on the IEL response of the detectors was also investigated. The charge collection of the diodes working in IEL mode was studied both before and after irradiation with a neutron fluence of $3x10^{11}$ n/cm^2 [28]. The diodes displayed excellent current voltage characteristics after neutron irradiation with more than 500V reverse bias being applied before breakdown and 100% charge collection occurring on a 3MeV proton beam [28]. These properties make them useful for simultaneous application for NIEL and IEL measurements at the same point in a phantom utilizing a paired detector method for separate component dosimetry in mixed radiation fields.

3 THE GEANT4 MONTE CARLO TOOLKIT

The Geant4 toolkit is a general purpose code developed by the CERN based RD44 collaboration for high energy particle physics applications. It is able to simulate the transport of many particle types and, in recent years, the capability to model low energy interactions has been added. This makes the GEANT4 toolkit useful for a variety of applications in radiotherapy physics [21]. It provides basic functionality of simulation as to describe detector geometry and materials, to transport particles, to describe detector response and to visualise simulation related information.

Geant4 is currently used in radiotherapy in order to verify treatment planning [23]. Starting from a CT image it is possible to perform a patient dedicated treatment plan to calculate the dose distribution in the target accurately [24]. Many other significant research activities, based on Geant4 studies, are in progress in the medical physics field both in diagnostic (e.g. PET) and therapy (e.g. IMRT and hadron therapy).

In dosimetric proton therapy studies both electromagnetic and hadronic interactions play a crucial role. Geant4 offers complementary and alternative physics models, to describe both these kind of processes [4].

Geant4 electromagnetic physics manages the electromagnetic interactions of leptons, photons, hadrons and ions over a wide energy range, spanning from 1 keV up to 1000 PeV. The physics processes modelled in Geant4 electromagnetic packages include: multiple scattering, ionization, bremsstrahlung, positron annihilation, photoelectric effect, Compton and Rayleigh scattering, pair production, synchrotron and transition radiation [37]. Two main packages handle alternative approaches to model the electromagnetic interaction of particles with matter: the Standard and Low Energy Package.

The Geant4 Standard electromagnetic package provides a variety of models based on an analytical approach, to describe the interactions of electrons, positrons, photons, charged hadrons and ions in the energy range from 1 keV – 10 PeV. The models

assume that the atomic electrons are quasi free; their binding energy is neglected except for the photoelectric effect; the atomic nucleus is assumed to be fixed and its recoil momentum is neglected [37].

The Geant4 Low Energy electromagnetic package extends the coverage of electromagnetic interactions in Geant4 below 1 keV, an energy range that is not covered by the Standard package, up to 100 GeV [37]. It handles the interactions of electrons, positrons, photons, charged hadrons, and ions, offering different sets of models for each of the physics processes involved.

Low energy processes are available to handle the ionization by hadrons and ions. Different models, specialized for energy range, particle type and charge, are provided. In the high energy domain (> 2 MeV) the Bethe-Bloch formula is applied; below 1 keV the interactions are described by the free electron gas model. In the intermediate energy range parameterized models based on experimental data from the ICRU.

The Geant4 hadronic physics component provides description of hadronic elastic and inelastic scattering for hadrons and ions. The basic requirements on the physics modelling of hadronic interactions in a simulation toolkit span more than 15 orders of magnitude in energy. The energy ranges from thermal for neutron cross-sections and interactions, through 7 TeV for LHC experiments, to even higher for cosmic ray physics. In addition, depending on the set-up being simulated, the full energy range or only a small part might be needed in a single application. The complex nature of hadronic showers and the particular needs of the experiment require the user to be able to easily vary the models for particular particles and materials depending on the situation [37].

The Geant4 hadronic package addresses the intrinsic complexity of this physics domain through a sophisticated software design. The design identifies the processes involved, such as, elastic or inelastic-scattering and defines a framework for the articulation of the different models implementing them. Models are characterized by

different conceptual approaches, by the energy range covered, and by specified features.

Data driven modelling is used in the context of neutron transport, photon evaporation, absorption at rest, and isotope production. The main data driven models in Geant4 deal with neutron and proton induced isotope production, and with the detailed transport of neutrons at low energies. The approach is limited by the available data to neutron kinetic energies up to 20 MeV, with extensions to 150 MeV for some isotopes [37]. The data driven approach is also used to simulate photon evaporation at moderate and low excitation energies, and for simulating radioactive decay.

Neutron fission and capture are described by means of parameterized model, as well as elastic scattering and inelastic final state production. The Bertini Elastic Scattering model is an alternative to the Parameterised elastic scattering [37].

Theoretical models are articulated over the various phases of nuclear interactions: nuclear de-excitation, pre-equilibrium, intra-nuclear transport, etc. Below 5 GeV centre of mass energy, intra-nuclear transport models are provided. For cascade type models, the alternative Binary cascade and Bertini model are available [37].

By using Object-Oriented technology and C++ code implementation, a powerful, flexible and extensible simulation toolkit has been created.

The Geant4 Monte Carlo toolkit requires the user to write his or her own C++ program using classes which inherent behaviour from kernel Geant4 classes. The kernel Geant4 classes are grouped in independent categories, with defined roles, as shown in Figure 3.1.

The classes which need to be implemented in developing a Geant4 application are described in the following sections.

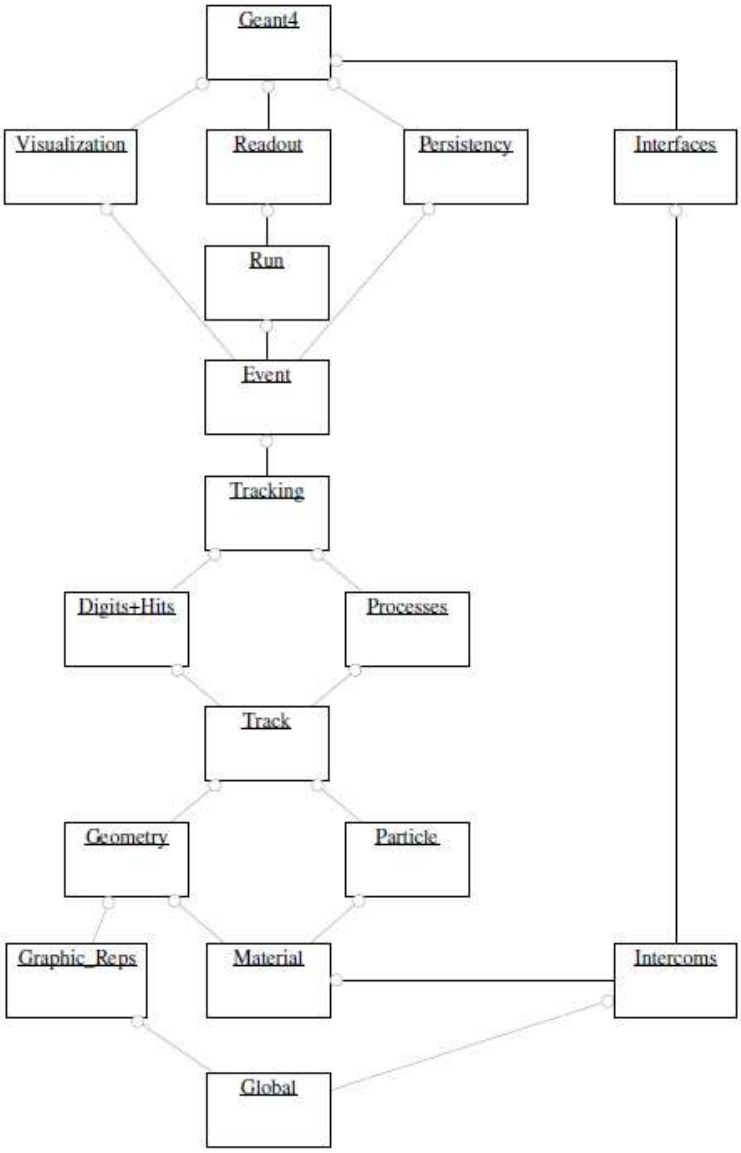

Figure 3.1 - The Top Level architecture of Geant4. The open circle represents a using relationship; the category at the end of the circle uses the adjoined category.

3. 1 **User Action Classes**

These are virtual classes whose methods control the geometry of the simulation, the definition of particles and their physics processes, and the generation of primary particles. They also control the flow of the simulation and allow the retrieval of useful information concerning track structure, interactions, energy depositions, etc., in the simulation experimental set-up.

3.1.1 G4UserDetectorConstruction

This base class controls the definition of the experimental set-up, in terms of geometrical components and material composition. A geometrical component is defined in terms of shape, material, position and rotation in the experimental set-up. Visualisation attributes can be defined at this level, to allow the visualisation of the experimental set-up. In a Geant4 simulation the detector is just a component of the experimental set-up, declared *sensitiv*e, where we can retrieve information about the *hits*. A *hit* is a snapshot of the physical interactions of a track in the sensitive region of the detector. The concept of a *track* represents physics information (position, energy deposition, mass, spin, etc.) of the particle under propagation [22].

3.1.2 G4VUserPhysicsList

There are three methods of this class which must be implemented.

The *ConstructParticle()* method defines all particles, involved in the experimental set-up. GEANT4 provides the implementation of all the particles defined in the Particle Data Group Book [38], however the particles involved in the experimental set-up of the simulation must be explicitly invoked in this method.

The *ConstructProcess()* method determines the models of interaction for these particles. All interaction processes are treated in the same manner from the tracking point of view; this enables the user to create a process and assign it to a particular

particle type. This transparency allows the customisation of physics processes by individual users.

The final method is *SetCuts()* which determines the threshold of production of secondary particles, expressed in range. If a secondary particle is generated with a residual range in the material less than this value, the particle will not be generated and tracked, but its energy will be considered locally deposited in the medium. Otherwise (residual energy > cut) the secondary particle will be generated and tracked.

To support the users, the Geant4 Collaboration provides examples of Physics Lists, realised within the Toolkit every six months, to be activated directly in the specific Geant4 application.

3.1.3 G4VUserPrimaryGeneratorAction

This class allows modelling of the radiation field investing the experimental set-up of the simulation, in terms of type of particle, polarisation, position, direction, energy, time. The number of primary particles to be generated in one event must also be defined. An *event* consists of a collection of primary particles to be tracked.

3.1.4 G4VUserEventAction

An *event* in Geant4 begins with the initiation of tracking one or more primary particle (as defined in the *PrimaryGeneratorAction*, see Section 3.1.3) and finishes with the completion of tracking all secondary's. The *G4VUserEventAction* class possesses two virtual methods which are invoked at the beginning and at the end of each event, the *BeginOfEventAction()* and the *EndOfEventAction()*, respectively.

3.1.5 G4UserRunAction

The concept of *run* in Geant4 is to keep a set of events to be simulated using the same detector geometry, the same event-generator and the same physics processes [22]. The *G4UserRunAction* class has several methods. One method that is commonly used is the *BeginOfRunAction()* method which is invoked before entering the simulation event loop. The second is *EndOfRunAction()* which is invoked at the very end of the event processing.

3.1.6 G4UserSteppingAction

The tracking category manages the propagation of a particle through the detector taking into account its physics interaction with matter.

The concept of a *step* in Geant4 describes the transport of a particle between two points in space. At this level the user can access information as energy, position, direction of the particle, energy deposition, etc.

3. 2 **Interface Commands**

Geant4 has various built-in user interface commands. These commands can be used interactively via a user interface (GUI), or in batch mode in a macro file. User defined commands can be implemented in user defined classes, inheriting behaviour from *G4UIMessenger* base class, which represents a messenger that delivers these commands to a class object. These commands are particularly useful when the geometry, primary beam, or physics parameters need to be altered between simulations. In this way one may execute several simulations using a macro file, containing a number of suitable commands, to change the experimental set-up ad hoc.

3. 3 **Visualisation**

Geant4 has the capability to visualise detector components, particle trajectories and tracking steps and hits of particles in detector components. Although many methods of visualisation are possible, the one employed in simulations of this thesis was the OpenGL driver. The OpenGL driver is most useful for visualising, with the aim of debugging, the generation of primary events and the tracking of these events through the geometry.

4 PIN DIODE EXPERIMENTAL CHARACTERISATION

One of the aims of this thesis is to experimentally characterise the forward bias response of the planar silicon PIN diodes and dedicated voltage read-out system under different conditions. This chapter outlines the investigation into the temperature dependence of the forward bias response of the PIN diode as well as the effect of light on this response and also the linearity of the pulsed current source in the dedicated forward bias read out system. All of these parameters are relevant to application of PIN diodes for separate neutron and proton dosimetry, out-of-field in proton therapy.

4. 1 **Introduction**

The temperature dependence of the PIN diode forward bias voltage was examined across the range of temperatures that may be encountered in the experimental environment for in phantom measurements on proton therapy facility. Any variance in forward bias response across this range of temperatures should be accounted for and a correction factor applied for accurate dosimetry.

The voltage across the junction in diodes with thin bases is proportional to the natural logarithm of the current density. That is, the familiar junction diode equation where current is proportional to $exp(eV/2kT)$ where e is the electronic charge, V is the voltage across the junction, k is Boltzmann's constant and T is the temperature. The effect of temperature on current density can be attributed to the thermal excitation of electrons from the valence band to the conduction band. This leaves vacant orbitals known as holes in the valence band which contribute to the conductivity. Thus, by increasing the temperature of the diode more electrons are excited into the conduction band and less bias voltage is needed in order to achieve a desired current. Diodes with long base lengths on the other hand are affected differently, a detailed description of long base diode forward bias response with change in temperature can be found in [39]. The effect of this change in temperature over the range from 25-35°C on the forward bias response of the diode in investigated in this chapter.

Due to the relatively low amount of energy required to produce an electron-hole pair in a semiconductor device (about 3 eV at room temperature [25]) in addition to thermal excitation, photons of visible wavelengths may also contribute to the conductivity. The visible light range consists of wavelengths ranging from 400 – 700 nm, corresponding to energies of 3.1 – 1.7 eV. Thus visible light may contribute to the conductivity of the device. The effect on the forward bias response of the PIN diodes when exposed to visible light is examined in this chapter in order to determine if an opaque encasing is required during experiments.

Some authors conducting experiments aimed at characterising silicon damage cross sections describe readers based on constant current sources [40], [41] whilst others describe investigating readers with pulsed current sources with a longer duration (approximately 10ms) [42]. Each of these studies found their method caused heating of their diode and subsequent annealing of radiation induced defects. The output of the system employed for the purposes of this research is described in Figure 4.1. The output is either 1 mA or 20 mA pulses for 100 µs at 100 Hz. This minimises any heating of the diode and annealing of the radiation defects during the readout. The linearity of the in-built constant current source in the dedicated forward bias read-out system developed at CMRP was investigated across a wide range of resistances.

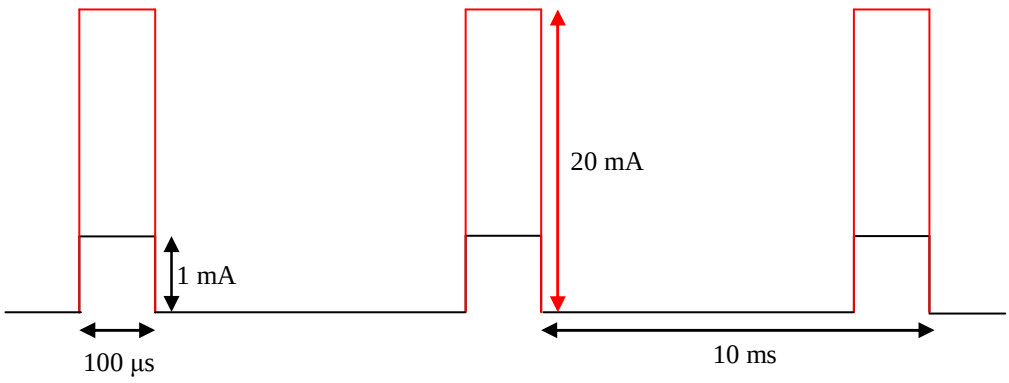

Figure 4.1 - The output of the in-built pulsed current source, with the 20 mA output shown in red and the 1mA output shown in black.

4. 2 **Methods**

4.2.1 Linearity of Pulsed Current Source

The linearity of the current source in the read-out system was tested at a number of different current values over a resistance range of 6.63kΩ - 12.1Ω to ensure that the current remained constant over these values. This experiment was performed to ensure that the response of the read-out system was constant for diodes of differing resistance.

The experimental apparatus used to perform the linearity measurements is shown in Figure 4.2. The resistors placed across the current source ranged from 6.63kΩ - 12.1Ω and currents of 1, 10, 15 and 20 mA were investigated. For each resistor the voltage was read directly from the display of the read-out system (with the inbuilt current source) and externally from a multi-meter. The current was then also measured by connecting a current probe to the current probe amplifier and then reading the output directly from a Cathode Ray Oscilloscope (CRO).

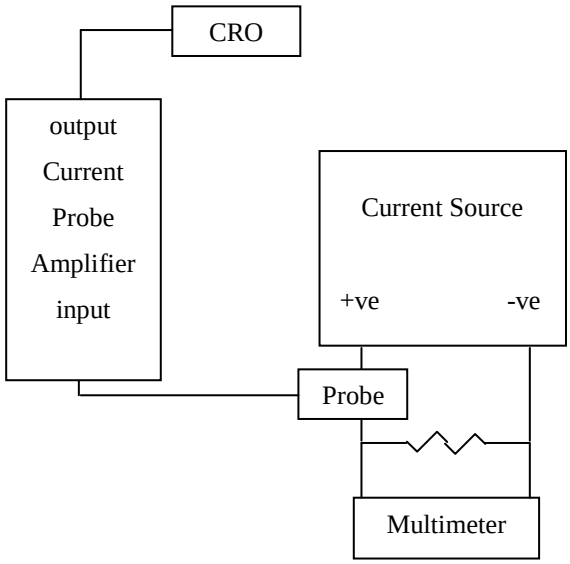

Figure 4.2– Experimental set-up for linearity measurements of pulsed current source for pin diode forward bias measurements.

4.2.2 Effect of Light Exposure on PIN Diode Response

The effect on the forward bias response of the PIN diodes when exposed to visible light was examined by first taking voltage measurements on each of the diodes using the dedicated forward bias voltage read out system at both 1 mA and 20 mA forward current with the diodes exposed to light. The measurements were then repeated with each of the diodes encased in a light tight box. These measurements were repeated five times. The differences between the forward bias voltage measurements with light exposed and light blocked were then examined whilst also taking into account variation between the individual measurements.

4.2.3 PIN Diode Temperature Dependence

To investigate any change in forward bias voltage across the temperature range of interest each of the PIN diodes forward bias voltage was measured at both 1 mA and 20 mA over a range from 25 - 35°C. This was achieved through the creation of a temperature controlled environment which was first heated to 40°C and allowed to cool down to room temperature (22°C). The temperature of the environment was measured using a digital thermometer with an accuracy of measurement of 0.1°C. The average cooling rate was approximately 0.5°C/min. This ensured that the thermometer, the diode and the surrounding environment were in thermal equilibrium. Depending on the base length, different theories of the effect of temperature on the forward bias response of the PIN diode can be applied, as discussed in [39].

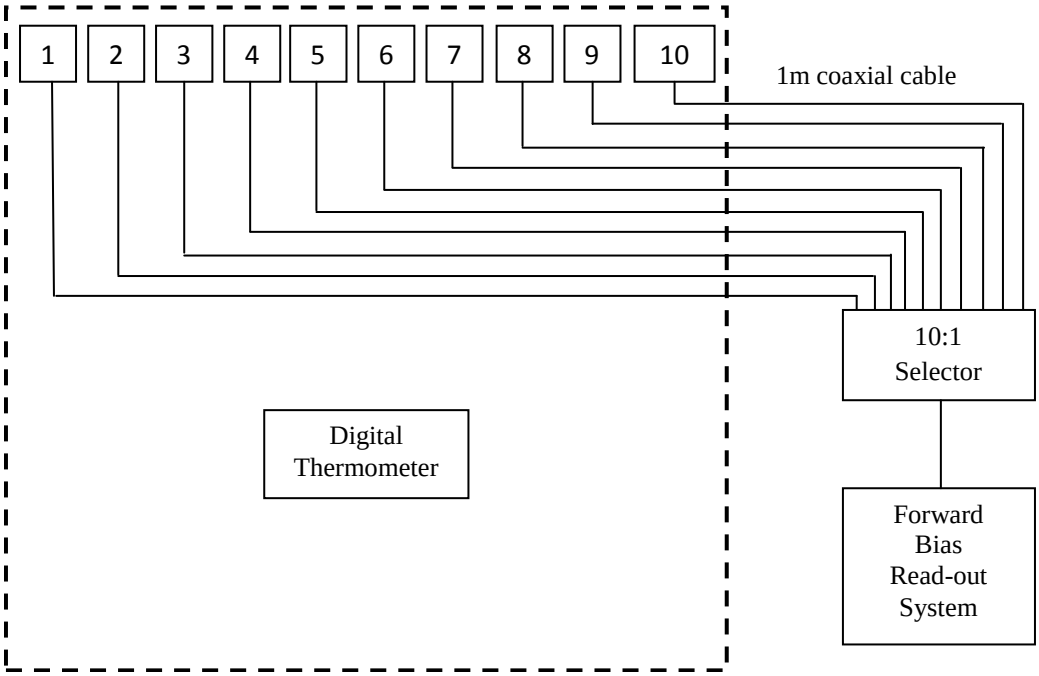

Figure 4.3– Experimental set-up for PIN diode temperature dependence measurements, the area of temperature control is indicated by the dashed line.

4. 3 **Results & Discussion**

4.3.1 Linearity of Pulsed Current Source

The linearity of the constant current source and accuracy of the forward bias voltage read out system were investigated using the experimental configuration described in Figure 4.2. Figures 4.4 - 4.7 show the forward voltage measured with both the voltage read out system and the externally attached multimeter as a function of resistance at 1mA, 10mA, 15mA and 20mA.

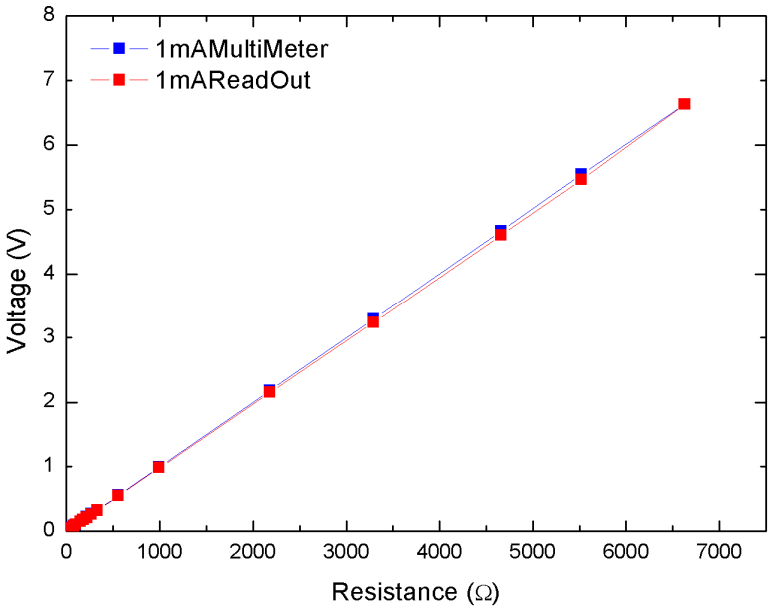

Figure 4.4– Forward Bias Voltage measured on the voltage read out system (red curve) and an externally attached multimeter (blue curve) at 1mA as a function of resistance.

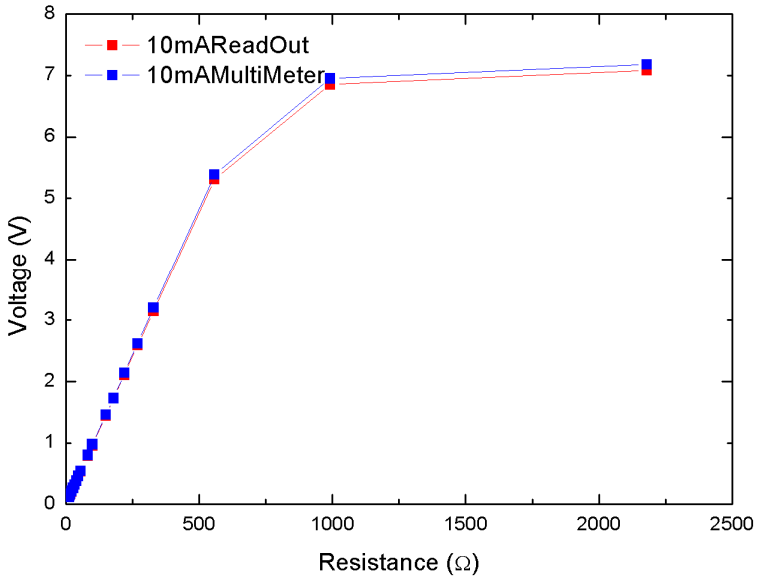

Figure 4.5 – Forward Bias Voltage measured on the voltage read out system (red curve) and an externally attached multimeter (blue curve) at 10mA as a function of resistance.

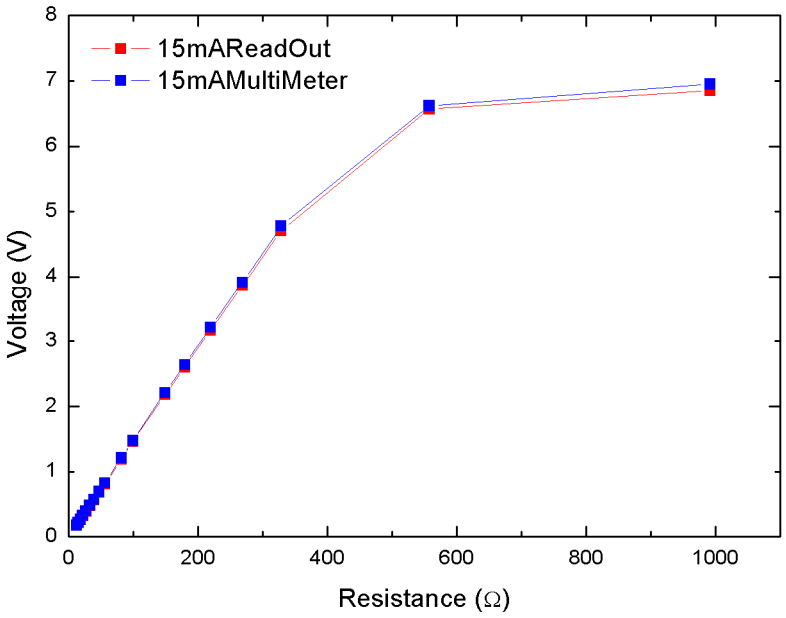

Figure 4.6 - Forward Bias Voltage measured on the voltage read out system (red curve) and an externally attached multimeter (blue curve) at 15mA as a

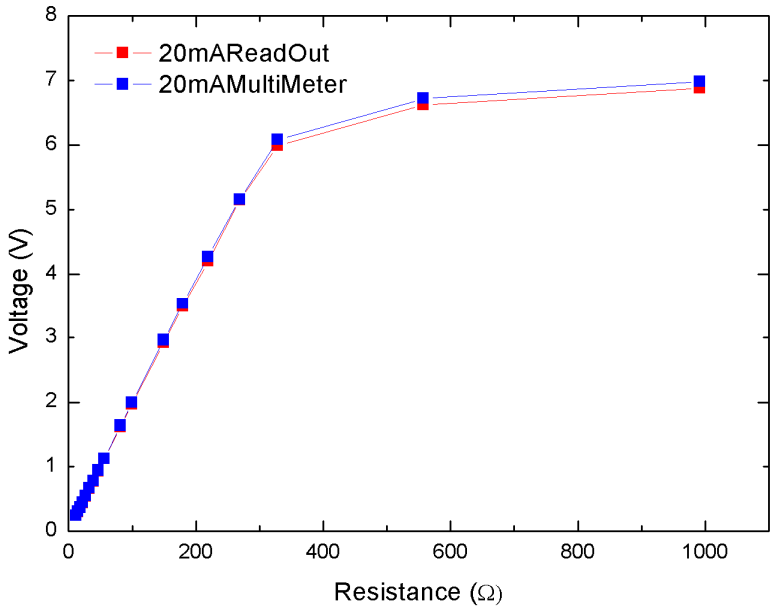

Figure 4.7– Forward Bias Voltage measured on the voltage read out system (red curve) and an externally attached multimeter (blue curve) at 20mA as a function of resistance.

From Figures 4.4 - 4.7 it can be seen that the forward bias voltage read-out system agrees well with the externally attached multimeter measurements over the range of resistances considered. A change in the linear relationship between voltage and resistance can also be seen in the Figures showing the 10, 15 and 20 mA characteristics (4.5 – 4.7). This change can be attributed to the fact that the current source is no longer putting out a constant value associated with 9V battery power supply used in this pulsed current portable reader.

The values of forward current measured on the CRO are shown in Figure 4.8 as a function of resistance. This Figure clearly shows the value of resistance at which each current value begins to change. In the case of 1 mA the output remains constant over the resistance range considered, the 10 mA curve shows a change at approximately 500Ω, the 15 mA curve at 330Ω and the 20 mA curve at 270Ω.

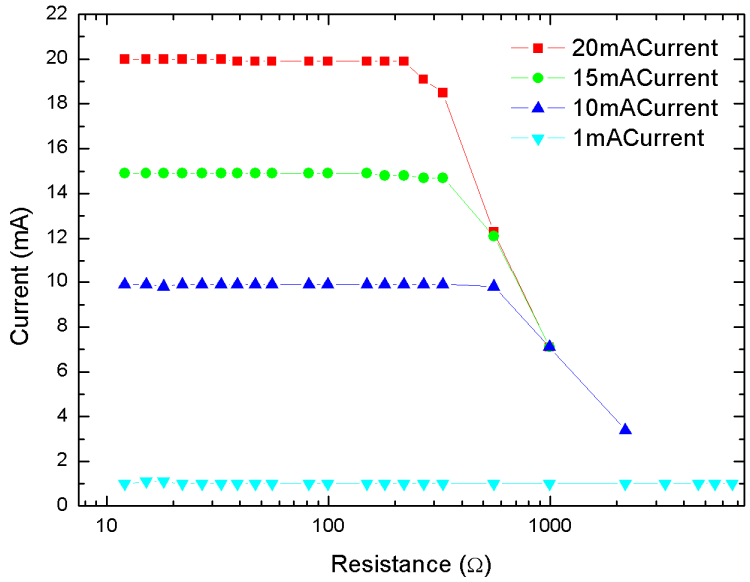

Figure 4.8– Output of the pulsed current source at 1, 10, 15 and 20 mA as a function of resistance.

This change in the value of current as the resistance is increased highlights the limit of power in the forward bias voltage read-out device. The device is powered by a 9V battery, with approximately 1.4V used to power components of the device such as the screen. This leaves approximately 7.6V available to power the pulsed current source. As the resistance is increased and more voltage is required to push the current through the device, the linear relationship between voltage and resistance no longer exists. This is due to the 7.6V limit of the device, and because of this the current begins to decrease and is therefore no longer constant.

Based on these experiments for used reader total change of the forward voltage for the diode should be not more than 7.6V to be sure that linearity of the response is not affected. This range is sufficient for planned experiments and allowed measurements of neutron absorbed TE dose about 3500cGy that is much more than expected for the purpose of our experiments. For out of field dosimetry, the relevant problem is increasing sensitivity of the diode in NIEL mode. This can be achieved, as mentioned, by increasing the length of the diode base or using increased readout current. We have developed and fabricated different planar PIN diodes with radial base lengths ranging from 0.2-1.2 mm corresponding to a neutron sensitivity range of 0.2-2.5mV/cGy (TE) neutron dose for 1mA readout current. A readout current of 20 mA will further increase this sensitivity.

4.3.2 Effect of Light Exposure on PIN Diode Response

The PIN diodes forward bias voltage were measured at a forward current of 1 mA and 20 mA with visible light exposed to the diodes and with diodes placed in a light tight box. Tables 4.1 – 4.3 summarise the results at both 1 mA and 20 mA for each of the planar silicon PIN diodes.

Detector	1mA (V)	20mA (V)	Uncertainty (V)
1	0.657	0.893	±0.001
2	1.035	1.718	±0.001
3	0.98	1.548	±0.001
4	1.001	1.605	±0.001
5	0.659	0.901	±0.001
6	0.797	1.093	±0.001
7	0.813	1.124	±0.001

Table 4.1– Forward bias voltage and uncertainties at 1mA and 20 mA with light exposed on the PIN diodes.

Detector	1mA (V)	20mA (V)	Uncertainty (V)
1	0.656	0.892	±0.001
2	1.035	1.717	±0.002
3	0.982	1.546	±0.003
4	1.001	1.605	±0.001
5	0.658	0.9	±0.002
6	0.799	1.094	±0.001
7	0.815	1.126	±0.003

Table 4.2– Forward bias voltage and uncertainties at 1 mA and 20 mA with light blocked from the PIN diodes.

Detector	Difference at 1mA (V)	Difference at 20mA (V)	Uncertainty (V)
1	0.001	0.001	±0.001
2	0	0.001	±0.002
3	0.002	0.002	±0.003
4	0	0	±0.001
5	0.001	0.001	±0.002
6	0.002	0.001	±0.001
7	0.002	0.002	±0.003

Table 4.3– Difference in forward bias voltage at 1 mA and 20 mA, compared to the uncertainty in these measurements.

Table 4.3 shows that the difference in forward bias voltage measurements with light incident on the diode and when light is blocked is no greater than the uncertainty involved in the measurement, using the dedicated forward bias voltage read-out system. As was shown in Figures the response of the forward bias voltage read out system is accurate over this voltage drop range. Thus the effect of visible light on the forward bias response of the planar silicon PIN diodes is negligible and there is

therefore no need to encase them in an opaque cover during experimentation. It is this fundamental difference between using PIN diode in NIEL mode and IEL mode where reverse current is affected strongly by light, and thus requires special packaging of the diode. An unpackaged diode has advantages as secondary particles (neutrons and protons in this case) are not affected by packaging and are based on phantom material only.

4.3.3 PIN Diode Temperature Dependence

The forward bias voltage was measured at a current of 1 mA and 20 mA at temperatures of 25, 28, 30, 32 and 35°C which is considered to adequately cover the possible operating temperature range of the dosimeters. The voltage versus temperature data for one of the diodes is shown in Figure 4.9.

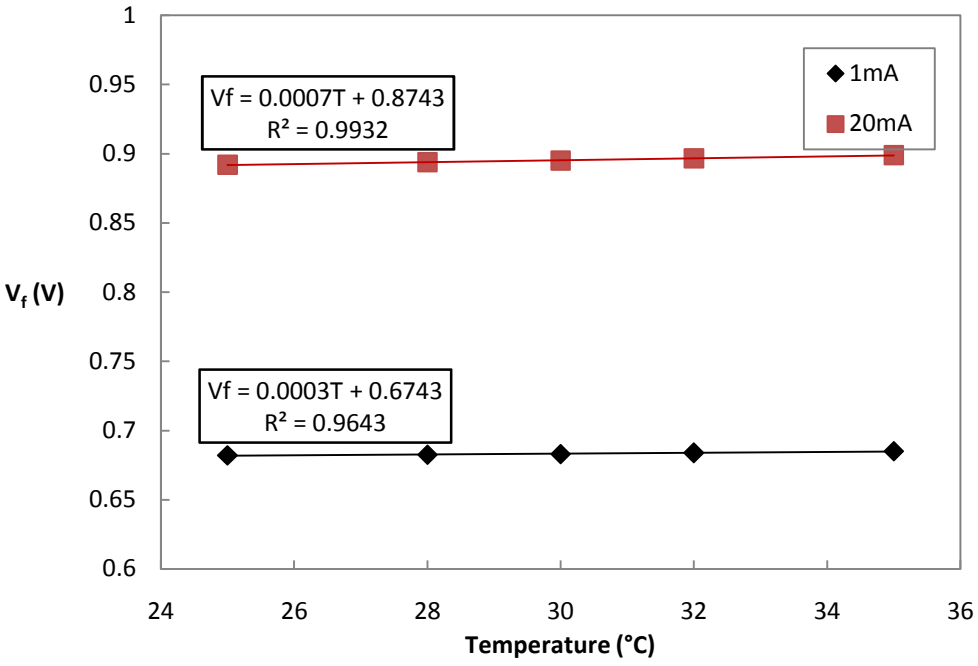

Figure 4.9– Forward bias voltage temperature characteristic of PIN diode dosimeter.

Measurements of the variation in forward bias voltage of the PIN diodes as a function of temperature were performed using a digital thermometer and dedicated

voltage read-out system in a temperature controlled environment. The average temperature coefficient was found to be 0.75mV/°C at 1mA and 1.8mV/°C at 20mA.

Taking into account that all measurements are aiming in a water phantom with real time readout before and immediately after irradiation we are expecting a change of temperature during irradiation much less then 1°C as a water phantom is a good thermostat. Thus, any small change in room temperature during the several hours between pre and post irradiation read out will not have any significant effect on the accuracy of the results. Also, because of this small temperature coefficient across the temperature range considered, the effect of base length on the type of coefficient produced is expected to be minimal.

5 SIMULATION OF PIN DIODE IN FIELD PROTON THERAPY RESPONSE

5. 1 **Introduction**

This chapter describes the investigation of the silicon PIN diode forward bias response in a proton therapeutic beam, for use in dosimetry in proton therapy. In particular the device was studied in-field, corresponding to central axis of the proton field in the region in the phantom, invested by the incident proton beam, along the Bragg peak (as described in Chapter 2.1).

In mixed proton and neutron fields both ionizing energy losses (IEL) and non-ionizing energy losses (NIEL) are important. NIEL are proportional to the bulk radiation damage in semiconductor devices resulting from displacement of atoms from their sites in the crystal lattice. For NIEL, the device effects are quantified in terms of displacement KERMA (kinetic energy released per unit mass) in silicon [1]. These displacement KERMA values in silicon are well documented for both protons and neutrons over a wide energy range [1]. When operated in forward bias mode the specially designed planar silicon pin diode described in Chapter 2.3.1 is sensitive to NIEL and almost insensitive to IEL.

Experimentally the macroscopic quantity measured in order to determine the damage imparted onto the PIN diodes is the forward bias voltage for a fixed small current. In principle it is possible to directly measure the change in carrier lifetimes by observing voltage decay across the diode irradiated by light pulsed source or switching the PIN diode from injection mode to reverse mode. This voltage decay represents the recombination of carriers close to the junctions and the slope of the curve allows the carrier lifetime to be determined. However this technique is not practical, and since the forward voltage of the PIN diode increases due to radiation degradation of the carrier lifetime, it can be used as a suitable monitor for NIEL [1].

As part of the investigation into this method of application, my study aims to simulate the PIN diode forward bias response placed in a water phantom as a

function of depth in a water phantom for number of typical proton therapy fields, by means of dedicated Monte Carlo simulations (Chapter 5.2).

5. 2 **Methods**

The Monte Carlo simulation application was written in C++, using classes which inherit behaviour from base classes of the GEANT4 toolkit [43]. The classes of the Geant4-based application manage different aspects of the simulation, such as: the experimental set-up (PIN diode detector and phantom), the radiation field, the particle interactions, and the actions carried out at the end of each particle event, output of the simulation (i.e. energy fluence of protons and neutrons in the PIN diode, necessary to calculate the silicon displacement KERMA). The gamma component was not important in our case due to the negligible effect on radiation damage of the diode.

The experimental set-up of the simulation is shown in Figure 5.1. Two different phantoms were used in the simulation study, each of the same geometry but with different compositions. The phantoms were made of water and Lucite alternatively. This choice was driven by the fact that Lucite (or Perspex) and water tank phantoms are commonly used in quality assurance procedures, at proton therapy facilities. These materials are considered an adequate approximation of human tissue, for dosimetric purposes. The composition of the phantom materials were made according to fraction by weight definitions given by NIST [12]. The phantoms were of dimensions 30 x 30 x 40 cm^3 to fully contain the incident proton beam.

The silicon PIN diode was modelled as 1cm x 1cm x 10 μm silicon block, placed in the phantom, with the 1 cm x 1 cm side facing the beam straight on. The silicon detector was placed at different depths along the Bragg Peak curve, in-field, as indicated in Figure 5.1.

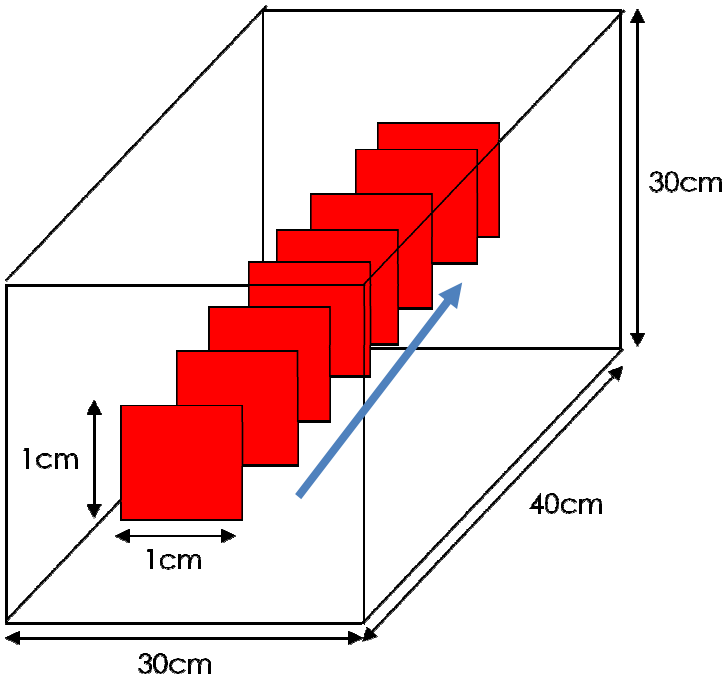

Figure 5.1- Experimental set-up adopted of the Geant4 application. The sensitive silicon block was placed at different depths within the phantom, in the configurations indicated by the red boxes. The phantom is made of water and Lucite alternatively. The primary field direction is indicated by the blue arrow.

The initial positions of the primary protons were randomly sampled on the surface of the phantom within the lateral dimensions of 5 x 5 cm^2. This model ignores the effect of the beam line components on the proton field and any interactions of the protons with beam modifying components; this is justified as for the purpose of this research only proton interactions within the phantom are of interest. The production of neutrons by nuclear reactions within the beam line can be reduced through the use of the spot scanning delivery method as described in Chapter 2.1.1, but neutrons produced by protons within the phantom (or patient) are unavoidable [8] .

The primary proton beam was modelled to be normally incident on the 30 x 30 cm^2 face of the phantom, 150 MeV and 225 MeV mono – energetic proton beams were considered. These beam energies were selected in order to match common experimental conditions, under study in my thesis. The 150 MeV beam energy is commonly used in paediatric and intracranial treatments [44] whereas the 225 MeV beam energy is commonly used for prostate treatments [45]. This model of radiation

field is simplified, as it does not consider the energy spread of the incident proton beam that is unavoidable in a passive beam delivery however practically negligible, but it retains the essential characteristics to study the suitability of PIN diodes as detector for mixed proton neutron fields, in proton therapy.

Because of the large difference in the energy of the two considered proton beams, the positions of the sensitive silicon volumes along the central axis were altered to account for the change in Bragg Peak position. Table 5.1 lists the positions where the silicon diode was set, along the Bragg peak, in each simulation. A total of 10^9 primary protons were used for each simulation, to produce statistically meaningful results.

150 MeV Lucite	**150 MeV Water**	**225 MeV Lucite**	**225 MeV Water**
2.5cm	2.5cm	2.5cm	2.5cm
5cm	5cm	10cm	10cm
8.5cm	8.5cm	15cm	15cm
10.5cm	10.5cm	21cm	21cm
11.5cm	12.5cm	25cm	25cm
12.5cm	13.6cm	26cm	28cm
13cm	14cm	26.25cm	29cm
13.25cm	14.5cm	26.75cm	30cm
13.5cm	15cm	27cm	30.5cm
13.613cm	15.25cm	27.403cm	31cm
13.85cm	15.76cm	27.8cm	31.5cm
	15.85cm		32cm
			32.5cm

Table 5.1– Positions of silicon volumes along the Bragg peak in each simulation.

The particle interactions modelled are based on a study by Jarlskog and Paganetti [20] that investigated and selected the Geant4 models which describe with the most accuracy the dosimetric measurements performed in proton therapy.

The G4EmStandard Package was selected to describe the electromagnetic interactions of photons, electrons, positrons, hadrons and ions. The energetic threshold of production of secondary particles was set equal to 1 keV, equal to the low energy limit of package model validity.

The G4BinaryCascade model was used to describe nuclear hadronic inelastic scattering of protons, neutrons, pions, up to 10 GeV. The G4LEPionPlusInelastic and G4LEPionMinusInelastic models were used to describe inelastic interactions up to 25 GeV for pion+ and pion– particles respectively. Also, the G4LEAlphaInelastic, G4LEDeuteronInelastic and G4LETritonInelastic models were used to describe inelastic scattering of alpha particles, deuterons and triton particles respectively. The hadronic elastic scattering was described by means of the G4UElastic Model. The simulation execution time was improved thanks to the adoption of the Geant4 *CutsPerRegion*, as shown in Figure 5.2. The delta electron tracks were simulated only in the region close to the detector, and in the detector itself, where the highest accuracy is required.

The goal of the simulation was to calculate the fluence of protons and neutrons, traversing the silicon diode, set at different depths, in the phantom, along the Bragg peak. The protons can be primary or secondary particles, generated by nuclear interactions. This information was then used to calculate the relative forward bias response of the PIN diode based on simulated silicon KERMA.

In the simulation, whenever a primary or secondary proton traverses the sensitive silicon volume, its kinetic energy was retrieved and stored into a histogram with range between 0 and 150 MeV, and bin width equal to 1 keV from 0.001 - 1MeV, and 1 MeV from 1- 150 MeV. These bin widths were chosen in order to match the values given for proton and neutron displacement KERMA in silicon from [1].

The forward bias mode PIN diode response was calculated for the proton and neutron fields, separately, along the Bragg peak, in order to evaluate and compare their contribution to the total response.

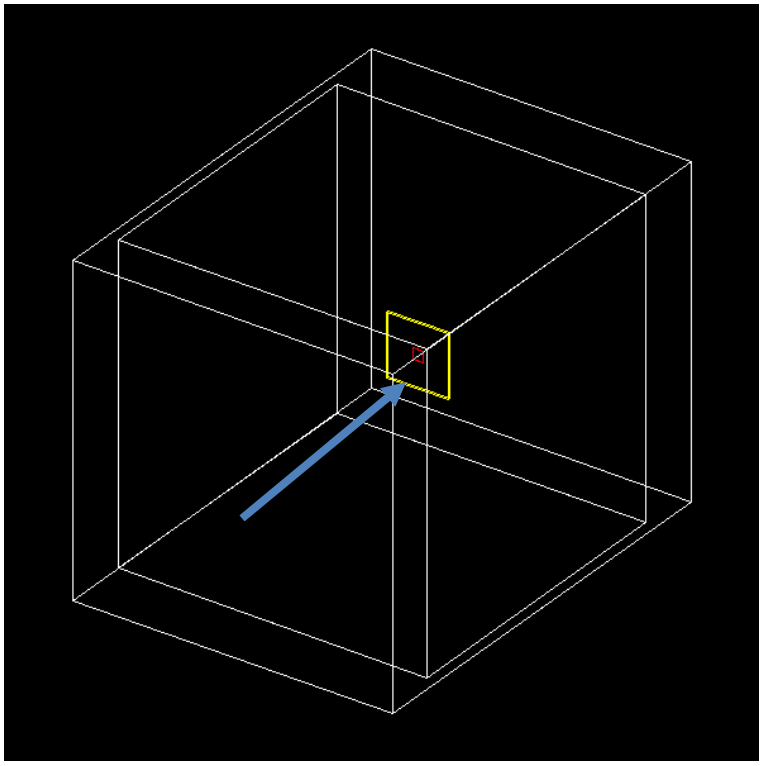

Figure 5.2– Detector geometry showing the residual range cuts by region. Charged particles produced within the red region have range cuts of 1μm, the yellow region has cuts of 10μm and the white region has cuts of 1mm. The primary field direction is indicated by the blue arrow.

The energy fluence of the protons (or neutrons) must be convolved with displacement KERMA values, according to Equation 8:

$$\Delta V_F = A \int \Phi_p(E_p) K_{Si}(E_p) dE, \tag{8}$$

where $\Phi_p(E_p)$ is the energy fluence and $K_{Si}(E_p)$ is the proton displacement KERMA values in silicon as a function of energy and A is a constant. In the case of the neutron energy fluence, the same equation (8) was used, but substituting $K_{Si}(E_p)$ with $K_{Si}(E_n)$ for neutrons.

A complementary Geant4 simulation study was addressed to the calculation of the dose distribution in the phantom, deriving from 150 and 225 MeV proton beams, to be used as a reference when discussing the suitability of PIN diodes for dosimetry, in proton therapy. The energy deposition was calculated in volumes with the same shape and size of the PIN diode, but with the same composition of the phantom (see Figure 5.3).

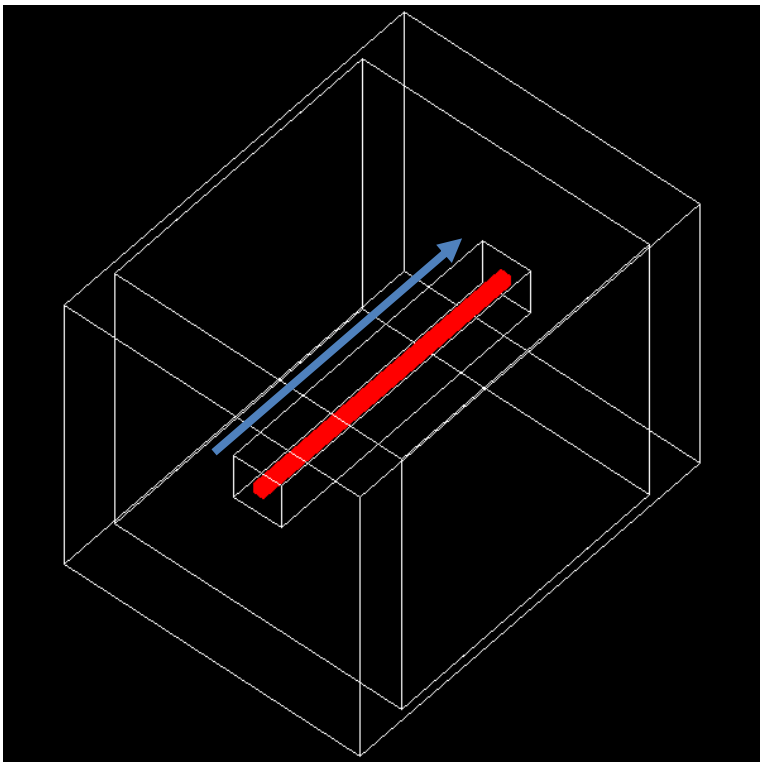

Figure 5.3 - The dose distribution along the Bragg peak was calculated in sensitive volumes (shown in red) – 1 x 1 cm^2- placed face to face along the central axis of the beam covering the entire length of the phantom. The sensitive detectors are made of water or Lucite, depending on the phantom configuration under study. The primary field direction is shown by the blue arrow.

5. 3 **Results & Discussion**

5.3.1 PIN Diode Forward Bias Response to Protons

The relative response of the PIN diode detector to protons in forward bias mode as a function of depth, along the Bragg peak, in the phantom, was simulated for the following configurations:

- 150 MeV protons incident on a Lucite phantom,
- 150 MeV protons incident on a water phantom,
- 225 MeV protons incident on a Lucite phantom,
- 225 MeV protons incident on a water phantom.

Figure 5.4 shows the proton fluence vs proton energy, along the central axis of the beam, at the entrance of the silicon diode, as a function of depth in the Lucite phantom, as a result of the simulation study. As expected, the average energy of the protons decreases with increasing depth as they interact with the phantom material. This also accounts for the decrease in fluence of the protons with increasing depth, as protons are scattered out from the central axis in nuclear interactions. When depths around the region of the Bragg peak are reached, as expected, the fluence consists of low energy protons and there is a larger spread in the energy distribution compared with shallower depths.

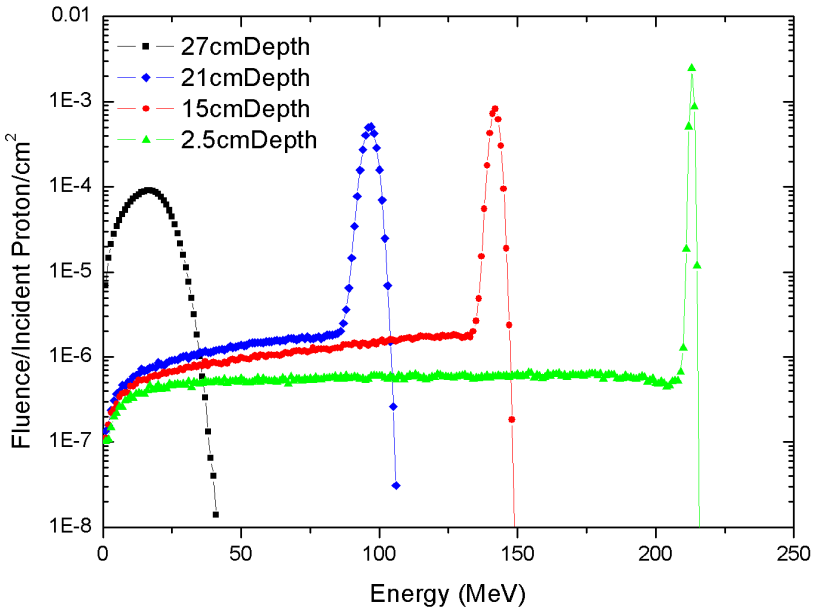

Figure 5.4 – Proton Energy Fluence/cm^2, per incident proton, shown at various depths in a Lucite phantom, as indicated in the legend. The results are affected with an uncertainty of 1%. The initial primary beam energy of the protons was 225 MeV, corresponding to a range of 32.61 cm.

The proton energy fluence curves, plotted in Figure 5.4, were convolved with the displacement KERMA values according to Equation 5 at each of the depths considered. These displacement KERMA values as plotted as a function of proton energy are shown in Figure 5.5.

The units of the displacement KERMA values are given in *D*/95MeVmB. *D* is the so called displacement damage cross-section of units MeVmB. Damage defects by energetic particles in the bulk of any material are proportional to this damage cross-section. 1 MeV neutrons are set to have a normalizing value D_n(1MeV) = 95MeVmB, thus the normalizing value given in Figure 5.5 is known as the radiation hardness factor. This quantity is responsible for displacements of atoms in the crystal lattice. The damage cross section, plotted in Figure 5.5 decreases rapidly at low proton energies before becoming approximately constant at energies approaching 100 MeV.

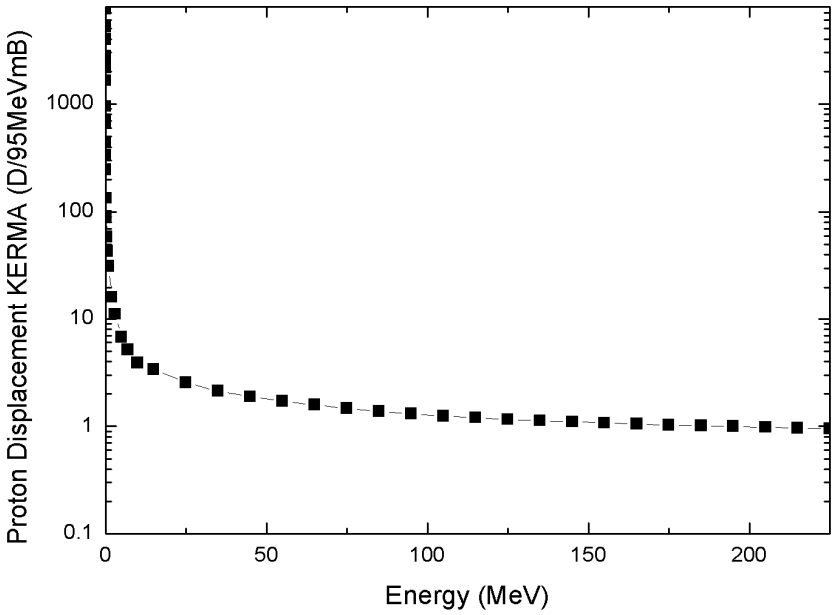

Figure 5.5 - The relative forward bias response of the PIN diode as a function of depth for each of the situations simulated.

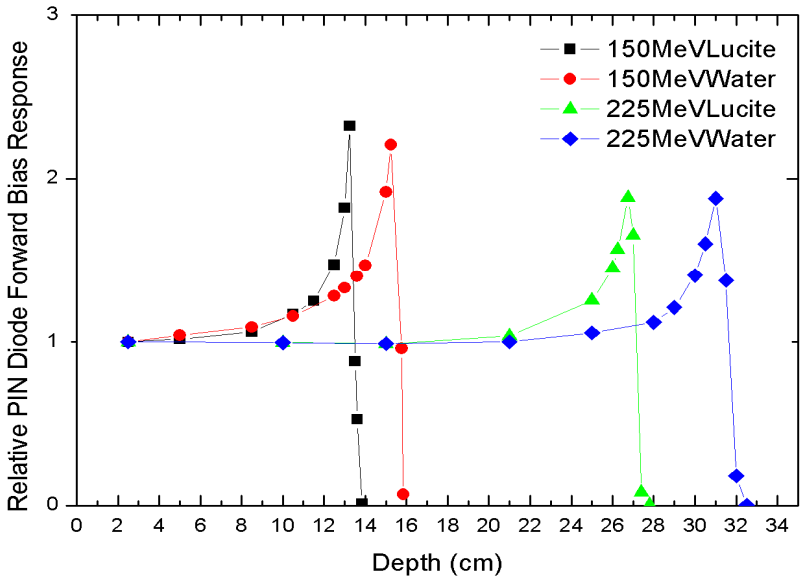

Figure 5.6 – Comparison of forward bias response of silicon PIN diode normalised to the depth 2cm to an uncertainty of 1% for each of the situations outlined in the legend.

5.3.2 Depth Dose Comparison

Figure 5.7 shows the dose distribution, in the phantom, calculated by means of Geant4. The proton ranges extrapolated from the Bragg peak curves were compared to the reference ICRU data [35]. The agreement obtained between the two demonstrates the accuracy of the model of the primary beam, of the phantom, and the physics component of the Geant4 simulation, from a software point of view. The range values calculated by means of the Geant4 simulation are approximately 50 μm. An error of 2% is estimated for the ICRU tabulated ranges [46]. Table 5.2 shows the comparison of the proton ranges calculated by means of Geant4 and ICRU data.

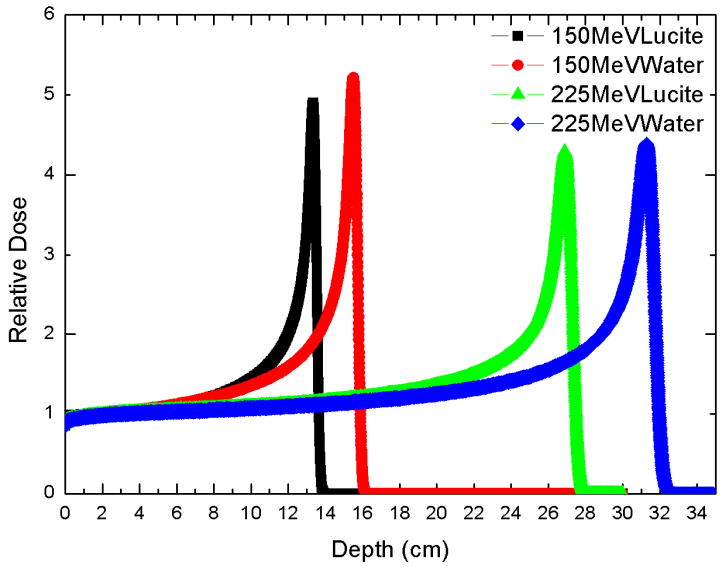

Figure 5.7 - Comparison of depth dose profiles to an uncertainty of 1% for each of the situations outlined in the legend. The energy deposition distribution was normalised at 2.5 cm depth, in the phantom.

Figures 5.8 – 5.11 show the comparison between the relative forward bias response of the PIN diode as a function of depth along the Bragg Peak, and the depth dose profile in the phantom, for each of the experimental configurations considered in the simulation study. The curves were normalised to a value of 1 at 2.5 cm depth which is the shallowest depth where the forward bias response was calculated.

	NIST Range (cm)	Geant4 Range (cm)
150 MeV Protons, Lucite Phantom	13.6 ± 0.3	13.5 ± $5x10^{-2}$
225 MeV Protons, Lucite Phantom	27.4 ± 0.6	27.3 ± $5x10^{-2}$
150 MeV Protons, Water Phantom	15.8 ± 0.3	15.7 ± $5x10^{-2}$
225 MeV Protons, Water Phantom	31.7 ± 0.6	31.7 ± $5x10^{-2}$

Table 5.2 – Comparison of range of primary protons from simulation study and NIST data.

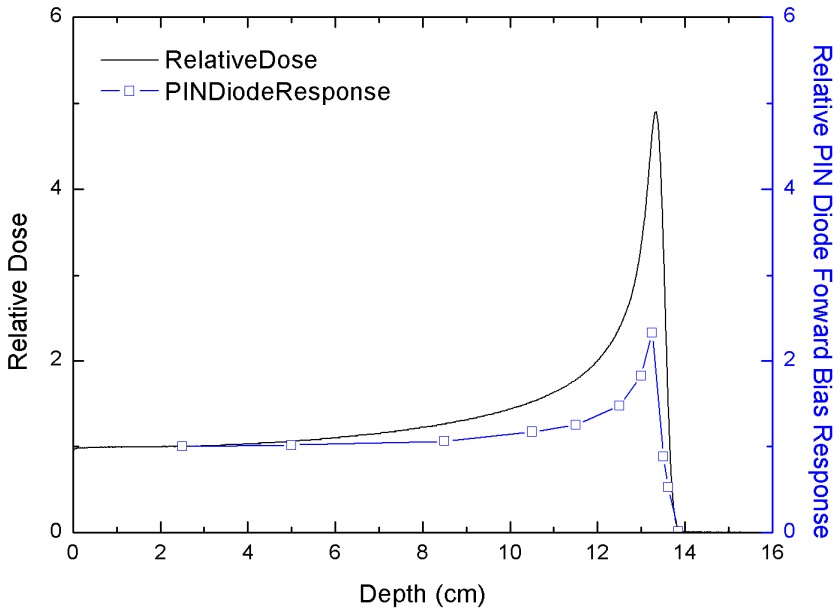

Figure 5.8– Relative forward bias PIN diode response comparison with theoretical depth dose distribution to an uncertainty of 1% in a Lucite phantom with 150 MeV primary beam.

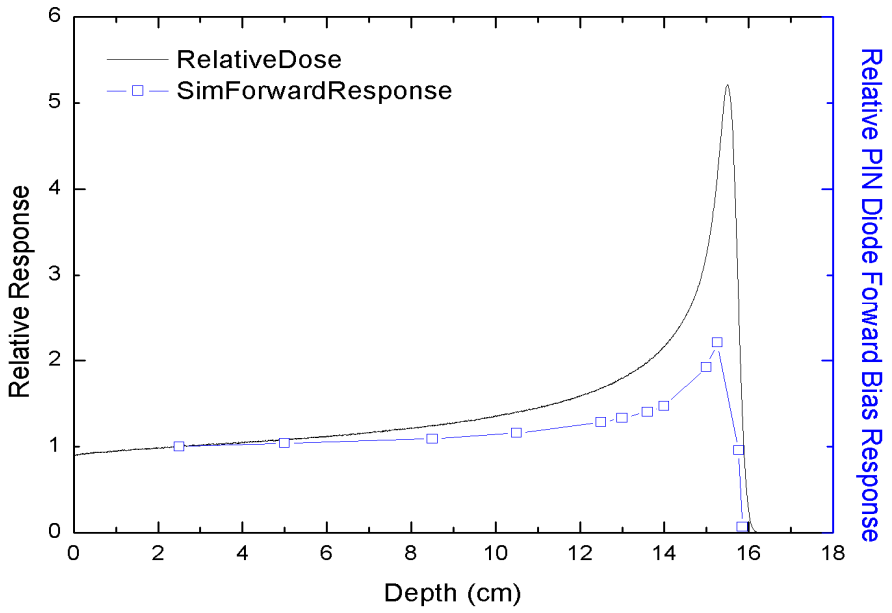

Figure 5.9 – Relative forward bias PIN diode response comparison with theoretical depth dose distribution with an uncertainty of 1% in a water phantom with 150 MeV primary beam.

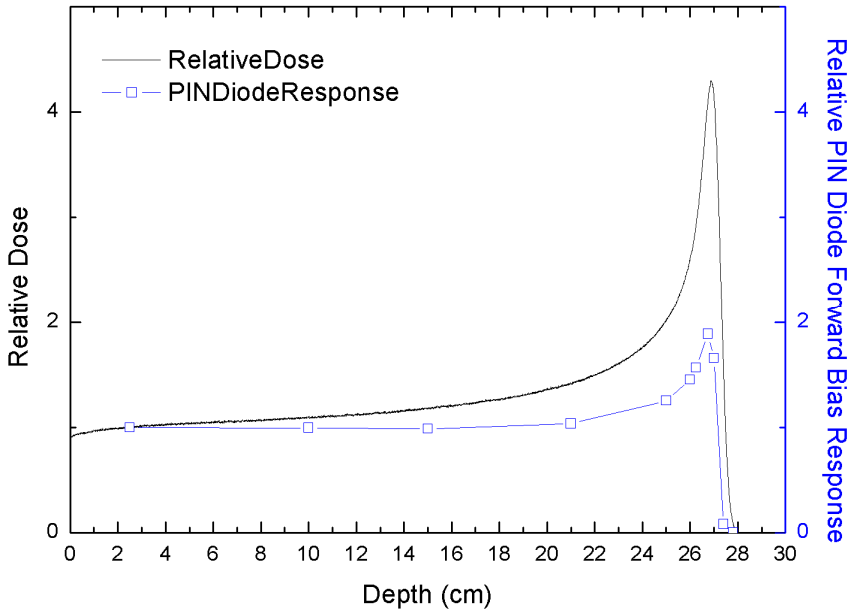

Figure 5.10 – Relative forward bias PIN diode response comparison with theoretical depth dose distribution with an uncertainty of 1% in a Lucite phantom with 225 MeV primary beam.

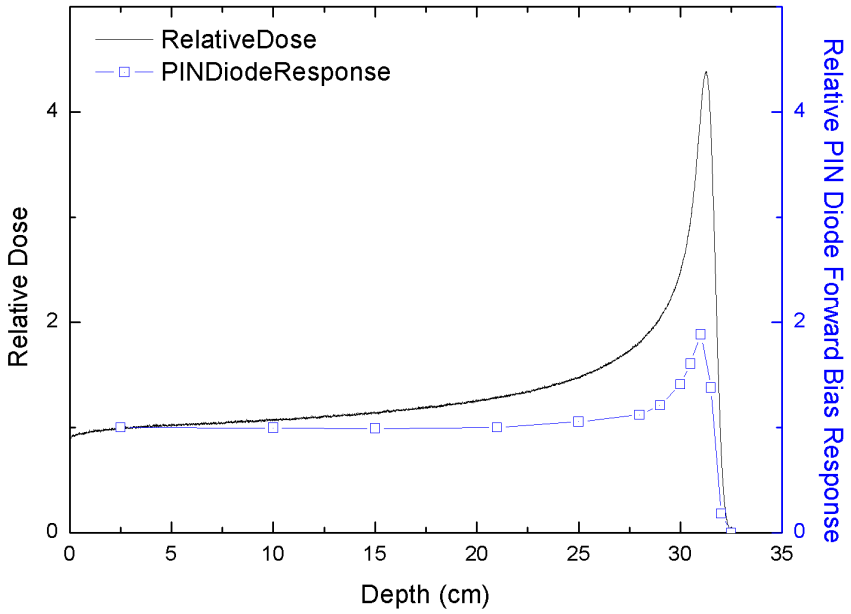

Figure 5.11 – Relative forward bias PIN diode response comparison with theoretical depth dose distribution, with an uncertainty of 1% in a water phantom with 225 MeV primary beam.

From Figures 5.8 - 5.11 it can be seen that the forward bias response of the silicon PIN diode as a function of depth does not match the depth dose distribution in the phantom. When the detector is operated in forward bias mode the response depends on the amount of damage KERMA (the displacement of atoms) in the detector, and not on the amount of energy deposited in the device. The depth dose profile depends mainly on the stopping power of the protons, whereas the forward bias response of the detector depends on the displacement KERMA.

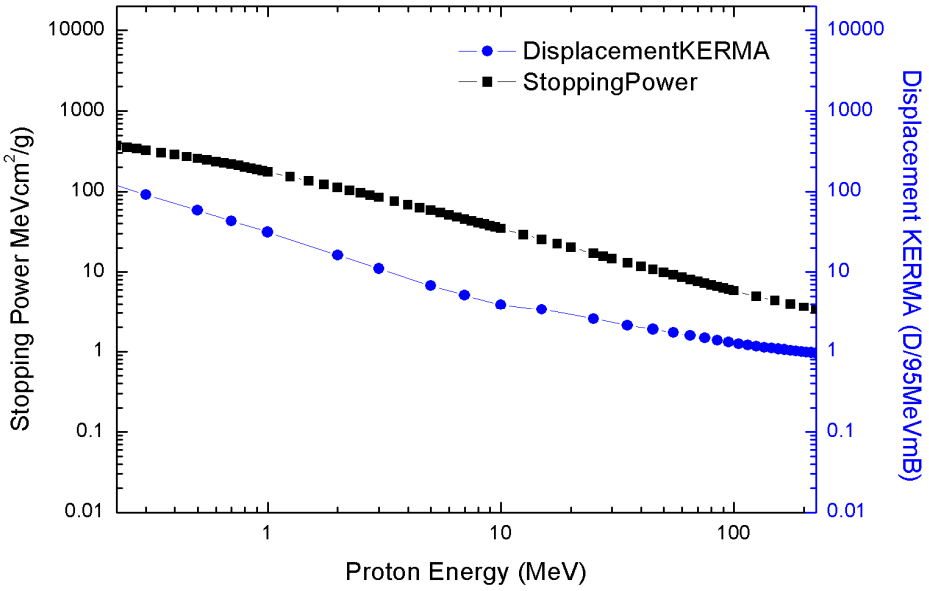

Figure 5.12 – Comparison of the change in electronic stopping power in silicon as a function of energy with the displacement KERMA in silicon as a function of energy.

When the stopping power is plotted along with the displacement KERMA as a function of energy, as shown in Figure 5.12, it can be noted that the stopping power increases more rapidly than the displacement KERMA at energies between 1 and 25 MeV. As shown in Figure 5.4 the fluence of protons in the Bragg peak region is comprised almost entirely of protons between these energies. Taking this into account it is now evident why there is an under-response of the PIN diode with depth along the central axis of the beam.

5.3.3 PIN Diode Forward Bias Response to Neutrons

As well as investigating the forward bias response of the PIN diodes to protons in field, the response to neutrons was also simulated. This was study was performed to evaluate the relative contribution of the total response of the PIN diode from protons and from neutrons. The response due to neutrons was simulated for the situation of a 150 MeV primary proton beam incident on a water phantom as well as a 225 MeV primary proton beam incident on a Lucite phantom. The same method that was used

for protons as outlined in Chapter 5.2 was used for the neutron simulation. Figure 5.13 shows how the neutron fluence changes with depth in the phantom.

As can be seen from Figure 5.13 the average neutron energy decreases with increasing depth in the phantom and the fluence of low energy neutrons remains relatively high across all depths. What is also evident is that there is an increase in the fluence of neutrons at intermediate depths in the phantom e.g. 10 cm and 15 cm depths.

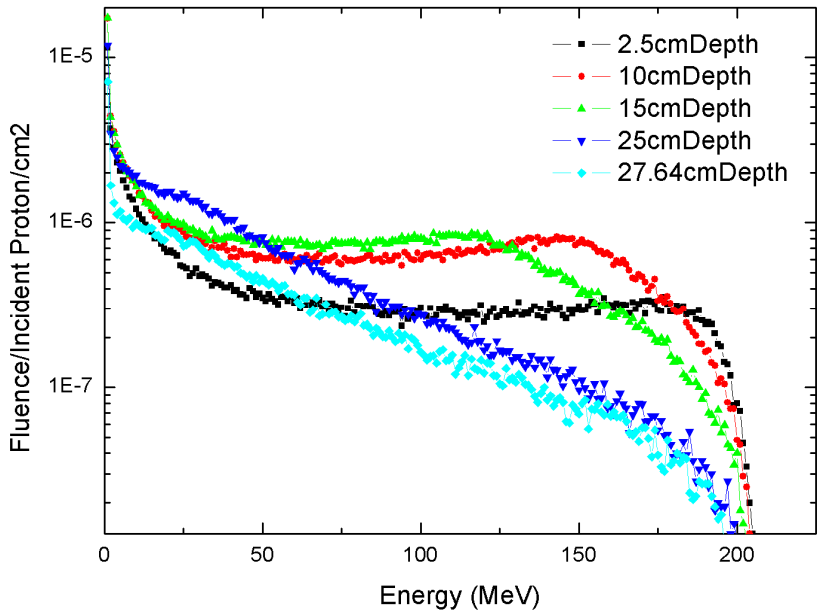

Figure 5.13– Neutron Energy Fluence/Incident Proton/cm2 shown at various depths in a Lucite phantom, with an uncertainty of 1%. The initial primary beam energy of the protons was 225 MeV.

These energy fluence curves were then convolved with the displacement KERMA values for neutrons in silicon [1]. These displacement KERMA values are plotted as a function of neutron energy in Figure 5.14. The units of collisional KERMA are the same as given for proton KERMA.

Figures 5.15 and 5.16 show the comparison of the PIN diode response in field due to neutrons and protons, in two experimental configurations under study. The response

of the PIN diode was calculated per incident proton and per cm^2 in order to compare accurately the response due to each particle.

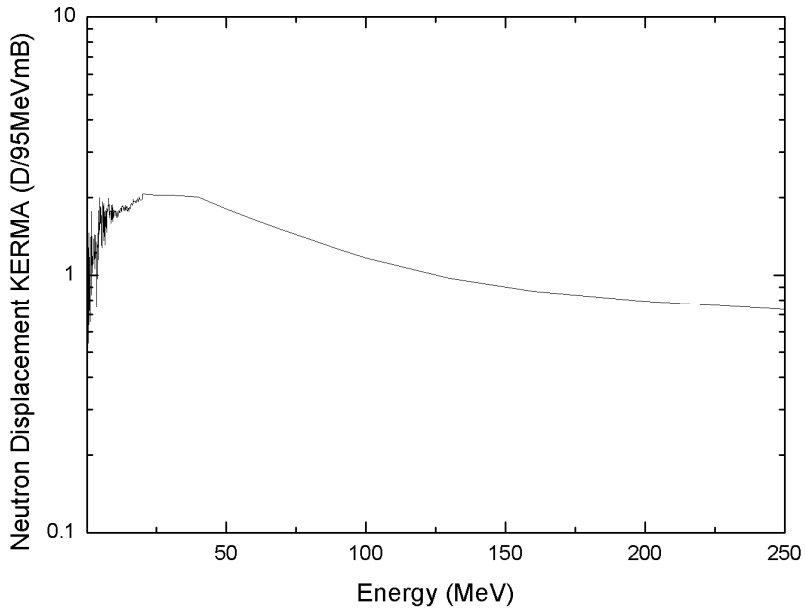

Figure 5.14 - Neutron Displacement KERMA values as a function of energy [1].

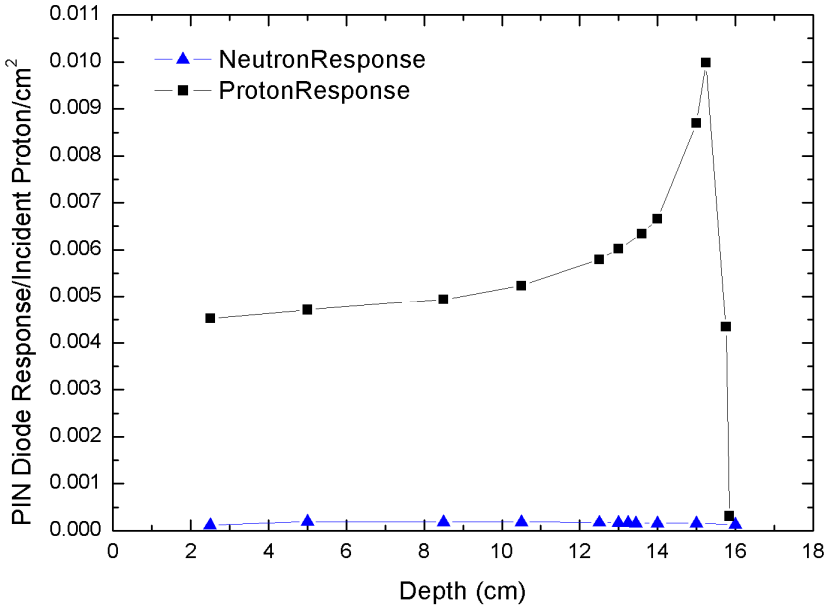

Figure 5.15 – Comparison of the PIN diode forward bias response due to neutrons and protons, with an uncertainty of 1% in a water phantom with a 150 MeV primary proton beam.

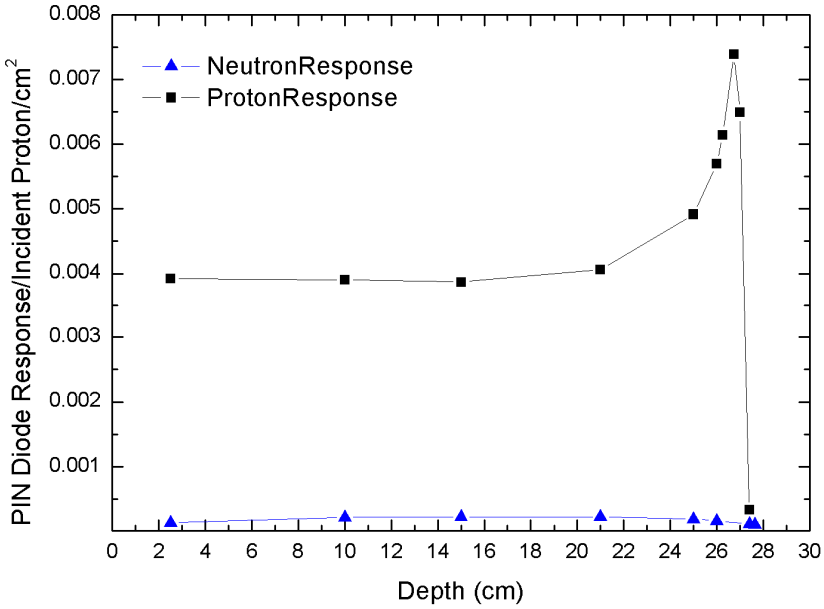

Figure 5.16 – Comparison of the PIN diode forward bias response due to neutrons and protons, with an uncertainty of 1% in a Lucite phantom with a 225 MeV primary proton beam.

As can be seen from Figures 5.15 and 5.16, the neutron contribution to the forward bias response of the PIN diode in field in proton therapy is extremely small, and the PIN diode is sensitive almost entirely to protons when placed in field. There is a small increase in the neutron response at intermediate depths due to the increase in neutron fluence but even at this point the neutron contribution remains below 5% of the total response.

When the response to both protons and neutrons is considered, that total change in forward bias voltage can be written as

$$\Delta V_f = \alpha D_n + \beta D_p, \tag{9}$$

where D_n and D_p are the respective neutron and proton absorbed tissue doses, α and β are constants and ΔV_f is the shift in forward voltage of the detector due to NIEL. As Figures 5.15 and 5.16 show, the neutron contribution, written as αD_n in Equation 9 is

negligible. Thus, when the diode is placed in field in proton therapy its forward bias response can be approximated to be

$$\Delta V_f \cong \beta D_p. \tag{10}$$

5.3.4 Calculation of Function β

The function β can be plotted with depth along the Bragg peak by dividing the forward bias response by the dose deposited. Figure 5.17 shows the plot of β for each of the situations considered, with results converted to water equivalent depths, achieved by multiplying by the respective depths by the density of Lucite. Thus, β is independent of the phantom material and depends only on the initial energy of the primary proton beam.

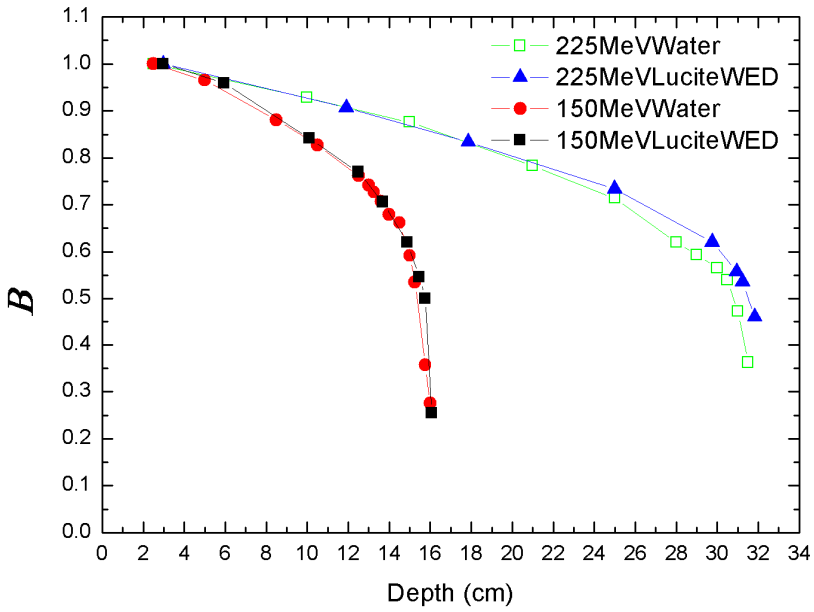

Figure 5.17 – β plotted as a function of depth with Lucite depths converted to water equivalent depths, with an uncertainty of 2%.

The function β is also able to be plotted as a function of proton energy, using the data shown in Figure 5.4. As the proton fluence at each depth is known, the average

energy at each depth can be calculated and plotted as a function of β, as shown in Figure 5.18.

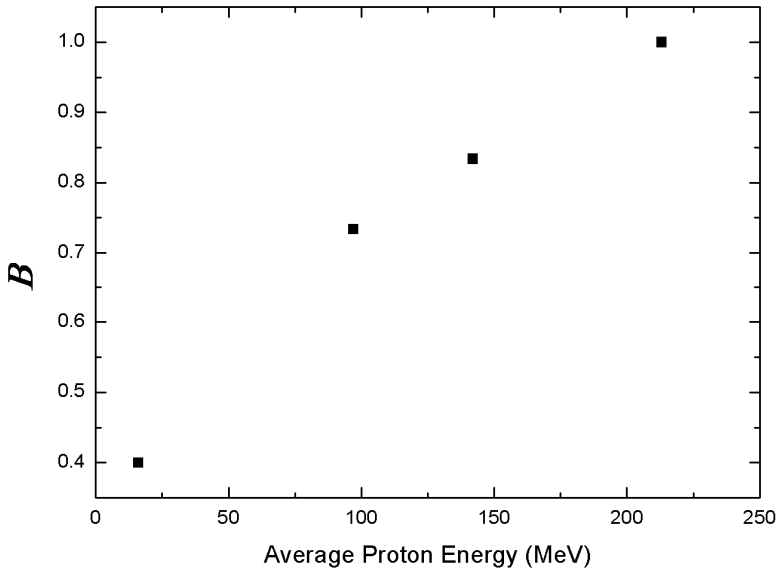

Figure 5.18 – β plotted as a function of average proton energy, with an uncertainty of 3%.

As can be seen from Figure 5.18, there is an approximate linear dependence of the β function with proton energy. By only using the average energy at each depth (as was done in Figure 5.18), proton energy straggling is ignored, this straggling increases with depth, as can be seen in Figure 5.4 and should be taken into account in future analysis. The response of the PIN diode is related to the spectra of protons and not just a single energy. However, Figure 5.18 does show that the calibration of PIN diodes can be performed along the central axis of the proton beam, provided information is known about the spectra of protons at each depth.

An article published by H. Paganetti [6] shows that protons are the major contributor to dose deposition in field in proton therapy. Figure 5.19 shows the percentage of the absorbed dose delivered by different particles for a 160 MeV proton beam incident on a water phantom in linear and in logarithmic scale summed over the lateral dimensions up to 3 cm from the beam centre. As the graphs show, the dose delivered in field is deposited almost entirely by primary and secondary protons. The largest

contribution other than protons being alpha particles responsible for 0.1% of the absorbed dose in field. Other particles such as ^{3}He ions, deuterons and tritons only contribute a percentage orders of magnitude less than this. The similarity between the results of secondary protons in Figure 5.18 and neutrons in Figures 5.15 and 5.16 can be attributed to the fact that secondary protons arise from interactions due to neutrons. The similarity between the two results adds to the validity of the simulation.

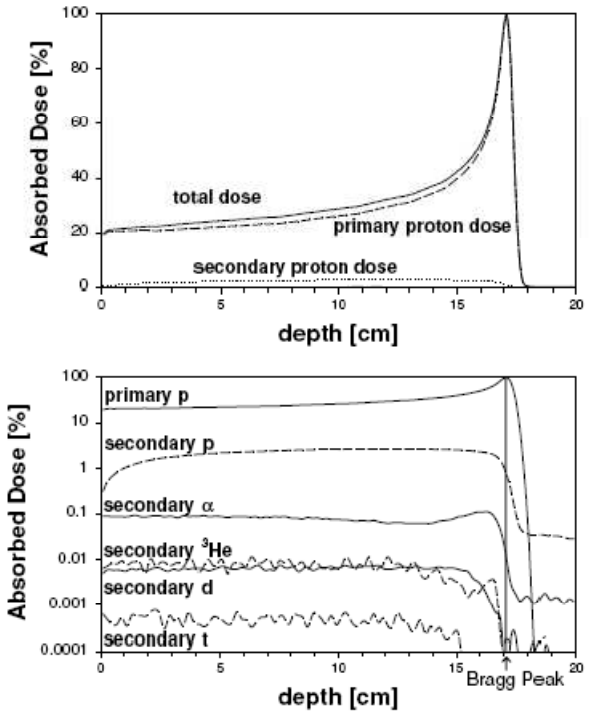

Figure 5.19 – Depth Dose distributions (Bragg peak normalized to 100%) for a 160 MeV proton beam incident on a water phantom. The upper figure shows the total dose and the dose due to primary and secondary protons. The lower figure compares, on a logarithmic scale, the doses due to different types of particles [6].

A consequence of this is that through measuring the total dose along the depth of the phantom, the assumption can be made that the dose measured is essentially the dose deposited by protons. Then, if β is known for specific proton energies (and water equivalent depths are used), through measuring the forward bias response of the PIN diode, it is possible to measure the dose deposited by protons as well as the response due to damage KERMA in the one measurement. Also, because of the absence of a

significant contribution to the total response of the PIN diode in field from neutrons, a calibration of the PIN diode forward bias response along the central axis of a proton beam is possible.

5.3.5 Experimental Comparison

Figure 5.20 compares the simulation results for the situation of a 150 MeV primary proton beam normally incident on a water phantom with experimental results from a similar situation. The PIN diodes used for the experimental measurements were irradiated at the KEK Proton Therapy Facility, Japan [47]. Measurements were performed in a water phantom along the central axis of a 150 MeV pulsed proton beam with the diode in a hermetically sealed sleeve. For comparison, measurements were taken with a charge sensitive commercial silicon PIN diode.

The proton therapy facility uses the KEK 500 MeV booster synchrotron as a beam source [47]. This source was originally designed for HEP experiments and since the energy and intensity are too high for medical applications, the beam energy is degraded down to 250 MeV using carbon based degraders; additional filters reduced this to 150 MeV. This synchrotron produces 50 ns pulses with an initial $2x10^9$ protons per pulse. The time interval between pulses is about 0.05 seconds for medical treatment. In full beam mode, the dose rate is about 200 cGy/min. The initial beam intensity is reduced by the carbon degrader followed by a collimator such that around 104 protons/pulse are transported to the medical beam line. Then the beam is momentum filtered and shaped to a 10 x 10 cm^2 field.

This beam presents a difficult experimental challenge even when using the small area of the silicon based PIN diode. Clearly, the high luminosity of this beam prevents the use of a proportional gas counter for microdosimetry due to strong pile up effects [48].

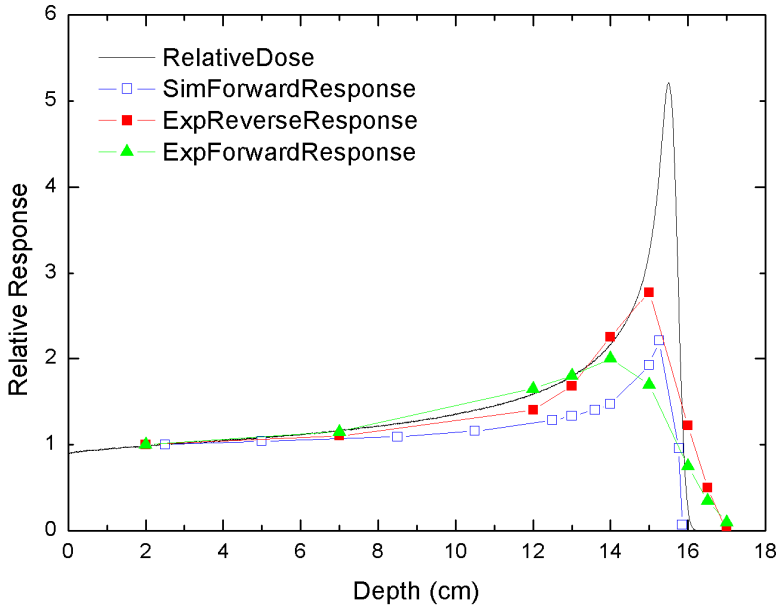

Figure 5.20 – Experimental comparison of the pin diode forward bias response for a 150 MeV primary proton beam in a water phantom, with an uncertainty of 1%.

The blue curve and green curve of Figure 5.19 show the simulated forward bias response and experimentally obtained forward bias response respectively. The peak to entrance ratio of the response is similar for both curves but the depth of the peak and the sharpness of the distal fall off do not agree well. These differences can be accounted for by considering that not only does the irradiation of the diode result in a change in carrier lifetime in the material but there is also a change in resistivity. This change in resistivity due to the fluence of protons and neutrons also results in a change in the forward bias response of the PIN diodes, this effect was not taken into account in the simulation study.

There are also some discrepancies between the black curve which shows the simulated depth dose response and the red curve which shows the response of a charge sensitive PIN diode with depth. The difference in the peak to entrance dose ratio between the two curves is due to the fact that particles produced in interactions with beam modifying devices were not considered in the simulation, these particles would contribute to the dose, with the possibility of decreasing the peak to entrance dose ratio of the simulated response. There is also a decrease in the sharpness of the

distal part of the beam in the experimental curve; this can be accounted for by the fact that in the simulation a ideal 150 MeV beam was considered whereas in the experiment there was a considerable spread in the beam energy due to the presence of the carbon based degraders and filters in placed in the beamline. Also, the use of diodes in the Bragg peak region of a proton beam are not ideal for depth dose measurements due to charge pile effects as a result of the high dose rate in the region [36].

The comparison highlights the need for more specific simulations when characterizing the response of the pin diodes in field in proton therapy. In order for an accurate comparison between the simulated and experimental results the simulation needs to take into account the proton beam line as well as the electronic specifications of the detector. Through simulation of the components of the beam line such as the scattering system and final collimators accurate beam characteristics can be reconstructed. Also, by taking into account detector characteristics such as noise and resolution in the detector response modelling, a more a more valid comparison can be obtained. This approach is supported by Geant4-based work published by Cirrone et. al. [49], on the dosimetric analysis of the hadron-therapy beamline of the Centro di AdroTerapia ed Applicazioni Nucleari Avanzate (CATANA). In this case the proton beam line elements, as the scattering system, the diagnostic monitor chambers, range shifters and final collimators, were included in the simulation experimental set-up. The response of a Markus chamber (for Bragg peak reconstruction) was also modelled specifically. The paper reports simulated proton range values and depth dose distributions to within 1.4% agreement with experimental results.

6 CONCLUSIONS AND RECOMMENDATIONS

6. 1 **Conclusions**

The dependence of the forward bias response of the silicon PIN diode on temperature was determined through experimental methods. It was found that across the temperature ranges commonly associated with laboratory environments the variation in the forward bias voltage at 1 mA and 20 mA was minimal. The average temperature coefficient calculated, given in mV/°C was found to be less than the limit of uncertainty in the measuring device. Thus, any small change in room temperature during the several hours between pre and post irradiation read out will not have any significant effect on the accuracy of the results.

The effect of visible light on the forward bias response of the silicon PIN diode was also investigated through experimental methods. Similar to temperature it was found that at both 1 mA and 20 mA the difference in forward bias voltage measurements with light incident on the diode and when light is blocked is no greater than the uncertainty involved in the measurement, using the dedicated forward bias voltage read – out system. Thus it was concluded that there is no need to encase the silicon PIN diodes in an opaque cover during experimentation.

The final experimental investigation examined the linearity of the current source in the dedicated forward bias voltage read – out system. It was found that the current remains constant over the range of resistances considered at 1 mA, to 500Ω at 10 mA, 330Ω at 15 mA and 270Ω at 20 mA. This change in the value of current as the resistance is increased highlights the limit of power in the forward bias voltage read-out device. The device is powered by a 9V battery, with approximately 1.4V used to power components of the device such as the screen, leaving approximately 7.6V available to power the pulsed current source.

The response of the silicon PIN diode was also characterised when placed in field during proton therapy through the means of Monte Carlo calculations on the Geant4

platform. The response was investigated for a number of different primary beam energies and phantom materials. It was found that the forward bias response of the detector due to protons was dependent on primary beam energy and phantom material through differences in range. It was also found that the forward bias response of the detector due to neutrons was negligible compared to that of protons.

The relative sensitivity of the device to protons was found by taking the ratio of the forward bias response of the detector due to protons with the dose deposited as a function of depth. This sensitivity was found to be dependent only on the primary beam energy when water equivalent depths in different phantoms were considered. The calibration of the PIN diode forward bias response along the central axis of a proton beam was also found to be possible.

Results from the Monte Carlo calculations were compared with those obtained from experiment, although the agreement between the two was not favourable. It was concluded that this was due to assumptions made during the simulations that did not reflect the experimental conditions accurately.

6. 2 **Recommendations**

The use of Monte Carlo calculations to further characterise the radiation field in proton therapy is strongly recommended. Although in order to correctly compare results obtained with those from experiments the simulations should model the experimental conditions with more accuracy than what was taken into account in this thesis. The radiation field present within the patient (or phantom) depends on the beam production method used due to the presence of secondary particles produced during interactions in the beam line and the spread in primary beam energy, both of which were not considered in this thesis. This change in radiation field will have an effect on the response of the detector and should be investigated further in future work.

The detector response and read – out electronics should also be investigated further in future work. Geant4 is purely a radiation transport code; it provides no insight into

how the change in resistivity of the silicon detector may influence the forward bias response. Also, the effect of modelling the detector dimensions more accurately during the Monte Carlo calculations could be investigated.

The use of Monte Carlo calculations as well as experiments to study the possibility of using the silicon PIN diodes in reverse bias for depth dose measurements could also be considered in future work. Through experimental methods such as Ion Beam Induced Charge Collection (IBICC), the charge collection characteristics of the diodes can be studied. Then through incorporating this information into Monte Carlo calculations, the suitability of the diodes for depth dose measurements can be determined. The effect of irradiation by hadrons when in forward bias on the charge collection properties and reverse bias breakdown voltage could also be investigated. This would allow for the use of combined forward and reverse bias measurements to more accurately separate and quantify the combined neutron and proton dose in proton therapy.

REFERENCES

1. Lindström, G. *Displacement Damage In Silicon*. 2000 [cited; Available from: http://sesam.desy.de/members/gunnar/Si-dfuncs.html.
2. Bonnett, D.E., *Current developments in proton therapy: a review.* Physics in Medicine and Biology, 1993. **38**(10): p. 1371-1392.
3. Academies, N.R.C.o.t.N., *Health risks from exposure to low levels of ionizing radiation - BEIR VII*. 2006: Washington DC.
4. Wroe, A.J., A.B. Rosenfeld, and R. Schulte, *Out-of-field dose equivalents delivered by proton therapy of prostate cancer.* Medical Physics, 2007. **34**(9): p. 3449-3456.
5. Wroe, A.J., I.M. Cornelius, and A.B. Rosenfeld, *The role of nonelastic reactions in absorbed dose distributions from therapeutic proton beams in different medium.* Medical Physics, 2005. **32**(1): p. 37-41.
6. Paganetti, H., *Nuclear interactions in proton therapy: dose and relative biological effect distributions originating from primary and secondary particles.* Phys. Med. Biol., 2002. **47**: p. 747-764.
7. Zheng, Y., et al., *Monte Carlo simulations of stray neutron radiation exposures in proton therapy.* Journal of Nuclear Materials, 2007. **361**: p. 289-297.
8. Schneider, U., et al., *Secondary Neutron Dose During Proton Therapy Using Spot Scanning.* Radiation Oncology Biol. Phys., 2002. **53**(1): p. 244-251.
9. Smith, A.R., *Proton therapy.* Physics in Medicine and Biology, 2006. **51**(13): p. R491-R504.
10. Agosteo, S., et al., *Secondary neutron and photon dose in proton therapy.* Radiotherapy and Oncology, 1998. **48**: p. 293-305.
11. Binns, P.J. and J.H. Hough, *Secondary Dose Exposures During 200MeV Proton Therapy.* Radiation Protection Dosimetry, 1997. **70**: p. 441-444.
12. Brenner, D.J. and E.J. Hall, *Secondary neutrons in clinical proton radiotherapy: A charged issue.* Radiotherapy and Oncology, 2008. **86**: p. 165-170.
13. Wilson, R.R., *Radiological Use Of Fast Protons.* Radiology, 1946. **47**(487).
14. Olsen, D.R., et al., *Proton therapy - A systematic review of clinical effectiveness.* Radiotherapy and Oncology, 2007. **83**(2): p. 123-132.
15. Jarlskog, C.Z. and H. Paganetti, *Risk of Developing Second Cancer From Neutron Dose in Proton Therapy as Function of Field Characteristics, Organ, and Patient Age.* Radiation Oncology Biol. Phys., 2008. **72**(1): p. 228-235.
16. Blattmann, H. and A. Coray, *A horizontal proton beam line for the development of a scanning technique.* Radiotherapy and Oncology, 1990. **17**(1): p. 17-20.
17. Kanai, T., K. Kawachi, and T. Hiraoka, *An irradiation facility and a beam simulation program for proton radiation therapy.* Nuclear Instruments and Methods in Physics Research Section A: Accelerators, Spectrometers, Detectors and Associated Equipment, 1991. **302**(1): p. 158-164.
18. Perez-Andujar, A., W.D. Newhauser, and P.M.D. Jr, *Neutron production from beam-modifying devices in a modern double scattering proton therapy*

beam delivery system. Physics in Medicine and Biology, 2009. **54**(4): p. 993-1008.

19. Yan, X., et al., *Measurement of neutron dose equivalent to proton therapy patients outside of the proton radiation field.* Nuclear Instruments & Methods in Physics Research, 2002. **476**: p. 429-434.
20. Jarlskog, C.Z. and H. Paganetti, *Physics Settings for Using the Geant4 Toolkit in Proton Therapy.* Nuclear Science, IEEE Transactions on, 2008. **55**(3): p. 1018-1025.
21. Rogers, D.W.O., *Fifty years of Monte Carlo simulations for medical physics.* Physics in Medicine and Biology, 2006. **51**(13): p. R287-R301.
22. Amako, K., *Present status of Geant4.* Nuclear Instruments and Methods in Physics Research Section A: Accelerators, Spectrometers, Detectors and Associated Equipment, 2000. **453**(1-2): p. 455-460.
23. Seco, J., et al., *A Monte Carlo tool for combined photon and proton treatment planning verification.* Journal of Physics: Conference Series, 2007. **74**: p. 021014.
24. Barca, G., et al., *A powerful simulation tool for medical physics applications: Geant4.* Nuclear Physics B - Proceedings Supplements, 2003. **125**: p. 80-84.
25. Knoll, G.F., *Radiation Detection and Measurement*. Third Edition ed. 2000: John Wiley & Sons.
26. Rosenfeld, A.B., et al., *Neutron and Proton Dosimetry with Improved Silicon Diodes.*
27. Rosenfeld, A.B., et al., *A System for Radiation Damage Monitoring.* IEEE Transations on Nuclear Science, 1999. **46**(6): p. 1766-1773.
28. Rosenfeld, A.B., et al., *Neutron Dosimetry With Planar Silicon p-i-n Diodes.* IEEE Transations on Nuclear Science, 2003. **50**(6): p. 2367-2372.
29. Rosenfeld, A.B., et al., *P-I-N Diodes with a Wide Measurement Range of Fast neutron Doses.* Radiation Protection Dosimetry, 1990. **33**: p. 175-178.
30. I. Anokhin, O.Z., A. Rosenfeld, M. Lerch, M. Yudelev, V. Perevertaylo, M. Reinhard, and M. Petasecca *Studies of the characteristics of silicon neutron sensors.* IEEE Transations on Nuclear Science, 2009. **56**(4): p. 2290-2293.
31. Khivrich, V.I.V., M.D. Litovchenko, P.G. Anokhin, A.I. Zinets, O.S. Reinhard, M.I. Rosenfeld, A.B. Carolan, M. Alexiev, D. , *High purity silicon as a basic material for manufacturing of radiation detectors and integral neutron dosimeters.* IEEE Transations on Nuclear Science, 1996. **43**(6): p. 2687-2692.
32. A.Rosenfeld, G.K., M.Carolan, B.Allen, O.Zinets , V.Khivrich, P.G.Litovchenko, *Application of P-I-N diodes and MOSFET for dosimeter in gamma and neutron fields.* Radiation Protection Dosimetry, 1999. **84**: p. 349-352.
33. M. Yudelev, K.A., J. Brandon, V. Perevertailo, M.Lerch, A. B. Rosenfeld *Application of semiconductors for dosimetry of fast neutron therapy beam.* Radiation Protection Dosimetry, 2004. **110**: p. 573-578.
34. F.Ravotti, M.G., A.B.Rosenfeld, M.L.F.Lerch, A.G.Holmes-Siedle, G.Sarrabayrouse, *Radiation monitoring in mixed environments at CERN: from the IRRAD6 facility to the LHC Experiments.* IEEE Transations on Nuclear Science, 2007. **54**: p. 1170-1177.
35. Berger, M.J. *Radiation Dosimetry Data*. 2009 [cited 2/2/2010]; Available from: http://www.nist.gov/physlab/data/radiation.cfm.

36. Rosenfeld, A.B., *Semiconductor Radiation Detectors in Modern Radiation Therapy*. Microdosimetric Response of Physical and Biological Systems. to Low –and High- LET Radiations: Theory and Application for Dosimetry, ed. Y.Horowitz. 2006: Elsevier.
37. Guatelli, S., *Radiation Shielding Analysis for the European Space Exploration Program*, in *Faculty of Science and Mathematics*. 2006, Univerity of Genova. p. 122.
38. *GEANT4*. [cited; Available from: http://wwwinfo.cern.ch/asd/geant4/geant4.html.
39. Swartz, J.M., Thurston, M.O., *Analysis of the effect of fast-neutron bombardment on the current-voltage characteristics of a conductivity modulated p-i-n diode*. Journal of Applied Physics, 1966. **37**(2): p. 745-755.
40. Speers, R., *Neutron Energy Dependence of Excess Charge Carrier Lifetime degredation in Silicon.* IEEE Transactions on Nuclear Science, 1968. **NS-15**(5): p. 9-17.
41. Youngblood, J.E. and W.R.V. Antwerp, *Calculated and Measured Displacement Damage in Silicon for Monoenergetic Neutrons.* IEEE Transactions on Nuclear Science, 1977. **NS-24**(6): p. 2521-2526.
42. Nagarkar, V., et al., *Solid State Neutron Dosimeter for Space Applications.* IEEE Transactions on Nuclear Science, 1992. **39**(4): p. 966-970.
43. Muzik, J., M. Soukup, and M. Alber, *Comparison of fixed-beam IMRT, helical tomotherapy, and IMPT for selected cases.* Medical Physics, 2007. **34**(5): p. 1580-1592.
44. Miralbell, R., et al., *Potential role of proton therapy in the treatment of pediatric medulloblastoma/primitive neuroectodermal tumors: Reduction of the supratentorial target volume.* International Journal of Radiation Oncology*Biology*Physics, 1997. **38**(3): p. 477-484.
45. Slater, J.D., et al., *Proton therapy for prostate cancer: the initial Loma Linda University experience.* International Journal of Radiation Oncology*Biology*Physics, 2004. **59**(2): p. 348-352.
46. ICRU, *ICRU Report 49*. 1993.
47. Matsuda, T. and K. Inamura, *Computer controlled multi-leaf conformation radiotherapy.* Nippon. Act. Radiol., 1981. **41**: p. 965 - 974.
48. Rosenfeld, A.B., et al., *A New Silicon Detector for Microdosimetry Applications in Proton Therapy.* IEEE Transactions on Nuclear Science, 2000. **47**(4): p. 1386.
49. Cirrone, G.A.P., et al., *Implementation of a New Monte Carlo-GEANT4 Simulation Tool for the Development, of a Proton Therapy Beam Line and Verification of the Related Dose Distributions.* IEEE Transactions on Nuclear Science, 2005. **52**(1): p. 262-265.